Tinyanont, S, Woosley, SE, Taggart, K, Foley, RJ, Yan, L, Lunnan, R, Davis, KW, Kilpatrick, CD, Siebert, MR, Schulze, S, Ashall, C, Chen, TW, De, K, Dimitriadis, G, Dong, DZ, Fremling, C, Gagliano, A, Jha, SW, Jones, DO, Kasliwal, MM, Miao, HY, Pan, YC, Perley, DA, Ravi, V, Rojas-Bravo, C, Sfaradi, I, Sollerman, J, Alarcon, V, Angulo, R, Clever, KE, Crawford, P, Couch, C, Dandu, S, Dhara, A, Johnson, J, Lai, Z and Smith, C

Supernova 2020wnt: An Atypical Superluminous Supernova with a Hidden Central Engine

The Astrophysical Journal, 951:34 (26pp), 2023 July 1 https://doi.org/10.3847/1538-4357/acc6c3

Supernova 2020wnt: An Atypical Superluminous Supernova with a Hidden Central Engine

Samaporn Tinyanont[1,2], Stan E. Woosley[1], Kirsty Taggart[1], Ryan J. Foley[1], Lin Yan[3], Ragnhild Lunnan[4], Kyle W. Davis[1], Charles D. Kilpatrick[5], Matthew R. Siebert[6], Steve Schulze[7], Chris Ashall[8], Ting-Wan Chen[4], Kishalay De[9], Georgios Dimitriadis[10], Dillon Z. Dong[3], Christoffer Fremling[3], Alexander Gagliano[11], Saurabh W. Jha[12], David O. Jones[13], Mansi M. Kasliwal[3], Hao-Yu Miao[14], Yen-Chen Pan[14], Daniel A. Perley[15], Vikram Ravi[3], César Rojas-Bravo[1], Itai Sfaradi[16], Jesper Sollerman[4], Vanessa Alarcon[1], Rodrigo Angulo[17], Karoli E. Clever[18], Payton Crawford[1], Cirilla Couch[1], Srujan Dandu[1], Atirath Dhara[1], Jessica Johnson[1], Zhisen Lai[1], and Carli Smith[19]

[1] Department of Astronomy and Astrophysics, University of California, Santa Cruz, CA 95064, USA; samaporn@narit.or.th
[2] National Astronomical Research Institute of Thailand, 260 Moo 4, Donkaew, Maerim, Chiang Mai, 50180, Thailand
[3] Division of Physics, Mathematics and Astronomy, California Institute of Technology, Pasadena, CA 91125, USA
[4] The Oskar Klein Centre, Department of Astronomy, Stockholm University, AlbaNova, SE-106 91 Stockholm, Sweden
[5] Center for Interdisciplinary Exploration and Research in Astrophysics (CIERA) and Department of Physics and Astronomy, Northwestern University, Evanston, IL 60208, USA
[6] Space Telescope Science Institute, 3700 San Martin Drive, Baltimore, MD 21218, USA
[7] The Oskar Klein Centre, Department of Physics, Stockholm University, AlbaNova, SE-106 91 Stockholm, Sweden
[8] Department of Physics, Virginia Tech, Blacksburg, VA 24061, USA
[9] MIT-Kavli Institute for Astrophysics and Space Research, 77 Massachusetts Avenue, Cambridge, MA 02139, USA
[10] School of Physics, Trinity College Dublin, The University of Dublin, Dublin 2, Ireland
[11] Department of Astronomy, University of Illinois at Urbana-Champaign, 1002 W. Green Street, IL 61801, USA
[12] Department of Physics and Astronomy, Rutgers, the State University of New Jersey, Piscataway, NJ 08854-8019, USA
[13] Gemini Observatory, NSF's NOIRLab, 670 N. A'ohoku Place, Hilo, HI 96720, USA
[14] Graduate Institute of Astronomy, National Central University, 300 Zhongda Road, Zhongli, Taoyuan 32001, Taiwan
[15] Astrophysics Research Institute, Liverpool John Moores University, IC2, Liverpool Science Park, 146 Brownlow Hill, Liverpool, L3 5RF, UK
[16] Racah Institute of Physics, The Hebrew University of Jerusalem, Jerusalem 91904, Israel
[17] Department of Physics and Astronomy, The Johns Hopkins University, Baltimore, MD 21218, USA
[18] Department of Biomolecular Engineering and Bioinformatics, Baskin School of Engineering, University of California, Santa Cruz, CA 95064, USA
[19] Ken and Mary Alice Lindquist Department of Nuclear Engineering, The Pennsylvania State University, University Park, PA 16802, USA
Received 2022 November 4; revised 2023 March 17; accepted 2023 March 17; published 2023 June 29

Abstract

We present observations of a peculiar hydrogen- and helium-poor stripped-envelope (SE) supernova (SN) 2020wnt, primarily in the optical and near-infrared (near-IR). Its peak absolute bolometric magnitude of -20.9 mag ($L_{\rm bol,\ peak} = (6.8 \pm 0.3) \times 10^{43}$ erg s^{-1}) and a rise time of 69 days are reminiscent of hydrogen-poor superluminous SNe (SLSNe I), luminous transients potentially powered by spinning-down magnetars. Before the main peak, there is a brief peak lasting <10 days post explosion, likely caused by interaction with circumstellar medium (CSM) ejected ∼years before the SN explosion. The optical spectra near peak lack a hot continuum and O II absorptions, which are signs of heating from a central engine; they quantitatively resemble those of radioactivity-powered hydrogen/helium-poor Type Ic SESNe. At ∼1 yr after peak, nebular spectra reveal a blue pseudo-continuum and narrow O I recombination lines associated with magnetar heating. Radio observations rule out strong CSM interactions as the dominant energy source at +266 days post peak. Near-IR observations at +200–300 days reveal carbon monoxide and dust formation, which causes a dramatic optical light-curve dip. Pair-instability explosion models predict slow light curve and spectral features incompatible with observations. SN 2020wnt is best explained as a magnetar-powered core-collapse explosion of a 28 $M_\odot$ pre-SN star. The explosion kinetic energy is significantly larger than the magnetar energy at peak, effectively concealing the magnetar-heated inner ejecta until well after peak. SN 2020wnt falls into a continuum between normal SNe Ic and SLSNe I, and demonstrates that optical spectra at peak alone cannot rule out the presence of a central engine.

Unified Astronomy Thesaurus concepts: Core-collapse supernovae (304); Massive stars (732); Dust formation (2269)

Supporting material: data behind figures

1. Introduction

Massive stars, $\gtrsim 8\,M_\odot$, conclude their evolution in many different variants of core-collapse supernovae (CCSNe). Stars that have lost their hydrogen envelope throughout their evolution, either via winds or binary interaction, produce a stripped-envelope (SE) supernova (SN), which shows little (Type IIb) to no sign of hydrogen (Type Ib) or helium (Type Ic) in their spectra around peak. Rapidly rotating stars may also undergo chemically homogeneous evolution (CHE), and lose hydrogen through nuclear burning. In the past two decades, a subclass of CCSNe, superluminous (SL) SNe, with a total

radiative energy about two orders of magnitude larger than that of a normal CCSN, has been discovered (e.g., Smith et al. 2007; Quimby et al. 2007; Ofek et al. 2007; Barbary et al. 2009), many of which aided by untargeted transient surveys (Quimby et al. 2011; Chomiuk et al. 2011; Nicholl et al. 2014; see reviews by Gal-Yam 2012, 2019.) While the threshold for a SLSN was initially demarcated at −21 mag (Gal-Yam 2012), later observations with a larger sample found that SLSNe form spectroscopic classes distinct from ordinary SNe (Inserra et al. 2013; Nicholl et al. 2014; Quimby et al. 2018; Lunnan et al. 2018; Angus et al. 2019), and that the two populations overlap in luminosity. Similar to ordinary SNe, SLSNe show two distinct classes with (Type II) and without (Type I) hydrogen. For hydrogen-rich SLSNe, interactions between the SN shock and circumstellar medium (CSM) can generally explain their luminosity and spectral properties (Chevalier & Irwin 2011), though other power sources may contribute (Inserra et al. 2018). The power source for hydrogen-poor SLSNe is more debated (e.g., Moriya et al. 2018).

Ordinary hydrogen-poor CCSNe (and also Type Ia SNe from explosions of white dwarfs in binary systems) are powered by the radioactive decay of ^{56}Ni and ^{56}Co. As such, the peak luminosity of these explosions is set by the total amount of ^{56}Ni produced, and the timescale of the light curve rise is set by the diffusion timescale of the ejecta, which is proportional to the total ejecta mass. In most SLSNe I, the peak luminosity is large but the light-curve rise is relatively short, such that the amount of ^{56}Ni required to power its peak equals or exceeds the total ejecta mass inferred from the rise time of the light curve (Gal-Yam 2012 and references therein).

To explain the extra luminosity observed, a central engine, such as a spinning-down magnetar (Kasen & Bildsten 2010; Woosley 2010) or an accreting black hole (MacFadyen et al. 2001; Dexter & Kasen 2013; Moriya et al. 2019), is often invoked to add energy into the SN ejecta. In the magnetar model, a magnetized neutron star with an initial period of $\sim$2 ms and magnetic field of $\sim 10^{14}$ G (Inserra et al. 2013; Nicholl et al. 2017) is born after the core collapse. It is coupled to the SN ejecta and spins down depositing its rotational energy into the SN ejecta, with a time-dependent rate of $L \propto t^{-2}$ (Ostriker & Gunn 1971), assuming a dipole radiation. In this model, it is crucial that the diffusion timescale of the SN ejecta and the magnetar spin-down timescale are roughly equal, allowing the magnetar heating to power a luminous peak (Inserra et al. 2013; Nicholl et al. 2017). Given this requirement, the region of the ejecta affected by magnetar heating is readily visible during the optically thick phase of the SN. As a result, spectroscopic signatures from the magnetar can be observed: most notably a hot blue continuum and W-shaped O II absorption series in the blue part of optical spectra (e.g., Mazzali et al. 2016; Quimby et al. 2018; Dessart 2019). While the magnetar model is generally successful at explaining observations of SLSNe (e.g., Inserra et al. 2013; Nicholl et al. 2017), there remain some unexplained features. Many SLSNe I show an early bump on a timescale of days after the explosion, likely from the shock-cooling emission from an extended envelope above the stellar surface (Piro 2015; Nicholl & Smartt 2016; Angus et al. 2019; Piro et al. 2021). Late-time light curves show bumps, which are unexpected from the power-law energy injection from a magnetar spin down and would require an additional power source, e.g., magnetar accretion and CSM interactions (Nicholl et al. 2016a; Inserra et al. 2017; Hosseinzadeh et al. 2022; Chen et al. 2023a). Recent population studies of SLSNe I observed by the Zwicky Transient Facility (ZTF) have found that about 20% of SLSNe I require earlier CSM interactions to fit their light curves (Chen et al. 2023a, 2023b). A small number of SLSNe I indeed show spectroscopic signatures of interactions with hydrogen-rich CSM at late times (Yan et al. 2015, 2017a; Chen et al. 2018).

Some spectroscopic SLSNe evolve slowly enough such that radioactivity could explain their light curves. If these SLSNe are truly powered by radioactivity, the ^{56}Ni mass required (a few solar masses) far exceeds what the standard neutrino-driven core-collapse mechanism can produce, which is about 0.2 $M_\odot$ observed in SNe II (Rodríguez et al. 2021) and SESNe (Lyman et al. 2016; Sravan et al. 2020). The only theoretically well-established physical mechanism that is able to produce such amounts of ^{56}Ni is the pair-instability (PI) process (e.g., Barkat et al. 1967; Rakavy & Shaviv 1967; Heger & Woosley 2002; Kasen et al. 2011).

PISNe happen in extremely massive stars with initial masses between 140 and 260 $M_\odot$ (Kasen et al. 2011). At the onset of carbon burning, the conditions in the core allow for rapid electron/positron pair production, which removes the radiation pressure support. As a result, the core collapses, igniting oxygen explosively and disrupting the star. The resulting PISNe are predicted to have a slow photometric evolution ($\gtrsim$100 days rise time) due to the large ejecta mass and distinct spectroscopic signatures due to its thermonuclear nature and low velocity. Thus far, a few slowly evolving SLSNe have been proposed as PISN candidates, e.g., SN 2007bi (Gal-Yam et al. 2009; but see Young et al. 2010). There are also a few other events evolving on a similar timescale, e.g., PTF12dam (Nicholl et al. 2013; Chen et al. 2015; Vreeswijk et al. 2017) and PS1-14bj (Lunnan et al. 2016). However, none of them have spectroscopic signatures consistent with PISN models (e.g., Dessart et al. 2012; Jerkstrand et al. 2016, 2017; Mazzali et al. 2019; Moriya et al. 2019). In general, these PISN candidates' spectra are too blue and the lines observed are too broad, and the nebular spectra show different abundance pattern from what is expected from a PISN. Because of the spectroscopic discrepancy, some have argued that these events could be core-collapse explosions, with novel explosion mechanisms, of very massive stripped stars (e.g., Mazzali et al. 2019; Moriya et al. 2019).

Peculiarities also exist in the spectroscopic SESN population. For instance, there are spectroscopic SNe Ib/c with late-time evolution inconsistent with a single radioactive power source. SN 2010mb (Ben-Ami et al. 2014) shows extra luminosity, blue pseudo-continuum, and narrow [O I] emission at late times, attributed to interactions with $\sim 3\,M_\odot$ of hydrogen-poor CSM. Other events, like iPTF15dtg, have a relatively long rise time and high peak luminosity, indicative of a large ^{56}Ni mass; but late-time observations show a power-law tail much better fit by a magnetar model (Taddia et al. 2016, 2019). Some multipeak events, like SN 2019stc, may require radioactivity, a magnetar, and CSM interactions to explain (Gomez et al. 2021). The diversity in the observed properties of hydrogen/helium-poor SNe is a manifestation of the different ^{56}Ni mixing, stripping mechanisms, CSM interactions, and the degree at which the newborn neutron star affects the resulting SN (e.g., Afsariardchi et al. 2021; Gomez et al. 2022; Sollerman et al. 2022). Peculiar events that probe

this vast range of SESN properties are still routinely being discovered.

Here, we present observations of SN 2020wnt, a hydrogen- and helium-poor SN with distinct photometric and spectroscopic properties. Its light-curve shape resembles that of SESNe, showing a relatively symmetric peak falling onto an exponential decline tail. However, the peak luminosity is much larger and the rise time is much longer than those of SESNe. Its spectroscopic evolution closely resembles that of SNe Ic up to about 1 year post peak with many marked differences compared to SLSNe. Late-time optical spectra, however, reveal features similar to magnetar-powered SLSNe. Late-time near-infrared (IR) observations reveal the formation of carbon monoxide (CO) and dust, similar to what is observed in SESNe and relatively novel for SLSNe. We recognize that while preparing this paper, Gutiérrez et al. (2022) posted their paper on the same SN on arXiv, presenting some similar observations and analysis; this work should be treated as an independent analysis on a largely independent data set (with only shared public ATLAS and ZTF photometry). In Section 2, we summarize the discovery and follow-up observations of SN 2020wnt. In Section 3, we analyze photometric data and compute explosion properties. In Section 4, we discuss the optical to near-IR spectroscopic evolution of SN 2020wnt, quantitatively comparing it to SESNe and SLSNe. In Section 6, we compare our bolometric luminosity to various models to discern the nature of SN 2020wnt. In Section 7, we compare our nebular spectra to model spectra to measure the properties of the ejecta. In Section 8, we discuss the stellar mass, star formation rate, and metallicity of the host galaxy. We provide a discussion and conclusion in Section 9.

2. Observations

2.1. Supernova Discovery and Classification

SN 2020wnt (ZTF20acjeflr) was discovered by the ZTF (Bellm et al. 2019; Graham et al. 2019; Masci et al. 2019) through the event broker Automatic Learning for the Rapid Classification of Events (Förster et al. 2021) on 2020 October 14 UT (Förster et al. 2020) (UT dates used hereafter). The discovery magnitude was $g = 19.7$. We decided to start following up this SN based on public light curves gathered by YSE-PZ, our Target and Observation Management System (Coulter et al. 2022). We classified SN 2020wnt as a Type I SN on 2020 November 16 using an optical spectrum obtained with the Kast spectrograph on the 3 m Shane Telescope at Lick Observatory (Tinyanont et al. 2020). All subsequent photometric and spectroscopic observations are also organized using YSE-PZ. The classification spectrum contained a narrow Hα emission from the host galaxy, putting the SN at $z = 0.0323 \pm 0.0001$. The corresponding luminosity distance is 141.8 Mpc, assuming a standard Lambda cold dark matter cosmology with $H_0 = 70\,\mathrm{km\,s^{-1}\,Mpc^{-1}}$, $\Omega_M = 0.3$, and $\Omega_\Lambda = 0.7$. At the time of classification, the transient had been brightening for a month. The Galactic extinction along the line of sight toward SN 2020wnt is $E(B-V) = 0.42$ mag (Schlafly & Finkbeiner 2011). We use this value for extinction correction throughout the paper, assuming $R_V = 3.1$ (Cardelli et al. 1989) and the extinction law of Fitzpatrick (1999). We assume that the host extinction is negligible owing to the lack of Na I D absorption at the host redshift.

2.2. Photometry

We obtained public forced photometry of SN 2020wnt from ZTF in the *g* and *r* bands, and from the Asteroid Terrestrial-impact Last Alert System (ATLAS; Tonry et al. 2018; Smith et al. 2020) in the cyan and orange bands. The SN was observed by these public surveys at a cadence of a few days.

These regularly scheduled photometry were supplemented by observations in the *griz* bands from the 2 m Liverpool Telescope on La Palma; *BVgriz* bands from the Lulin One-meter Telescope (LOT) at the Lulin Observatory in Taiwan; and *BVri* bands from the 1 m Nickel telescope at Lick Observatory in California. These observations were reduced using standard optical imaging procedures: bias and flat-field correction and photometric calibration using stars observed in the same field of view.

We analyzed the *griz* imaging from the LOT and the *ri* imaging from the Nickel telescope using image frames from the Pan-STARRS 3π survey (Flewelling et al. 2020) as templates. After registering and estimating a zero point for each LOT image in `photpipe` (Rest et al. 2005), we performed digital image subtraction between each LOT and Pan-STARRS image using `hotpants` (Becker 2015). We then performed forced photometry at the location of SN 2020wnt using a custom version of `DoPhot` (Schechter et al. 1993).

We obtained ground-based near-IR imaging of SN 2020wnt on 2021 August 19 using the slit-viewing camera of the SpeX spectrograph (Rayner et al. 2003) on the NASA InfraRed Telescope Facility (IRTF) in the *J*, *H*, and *K* bands. The data were reduced using a custom `python` script that constructed the sky flat image from the dithered observations, performed flat-fielding and background subtraction, then shifted and coadded observations in each band. We obtained another epoch of near-IR photometry on 2021 December 10 using the Near-InfraRed Imager (NIRI) on Gemini North in the *J*, *H*, and *Ks* bands as part of the fast-turnaround program GN-2021B-FT-109 (PI: Tinyanont). We used `DRAGONS v.3.0.1` to reduce NIRI images; the steps were similar to the script we used to reduce the IRTF images. Photometric calibration in both cases were obtained using Two Micron All Sky Survey (Milligan et al. 1996; Skrutskie et al. 2006) stars in the field of view.

In addition to ground-based observations, we observed SN 2020wnt with the Ultra-Violet and Optical Telescope (Roming et al. 2005) on board the Neil Gehrels Swift Observatory (Gehrels et al. 2004) at 46, 98, 118, 138, and 158 days post discovery in the *U*, *B*, *V*, *UVW1*, and *UVW2* bands. The data were processed by the standard data-reduction pipeline and obtained via the HEASARC archive. We did not detect the SN in the *UV* bands. Aperture photometry was obtained using a 3″ radius aperture centered on the SN with local background subtraction.

SN 2020wnt was observed during the ongoing Near-Earth Object Wide-field Infrared Survey Explorer (NEOWISE) all-sky mid-IR survey in the W1 (3.4 μm) and W2 (4.5 μm) channels (Wright et al. 2010; Mainzer et al. 2014). We retrieved time-resolved coadded images of the field created as part of the unWISE project (Lang 2014; Meisner et al. 2018). To remove contamination from the host galaxies, we used a custom code (De et al. 2020) based on the ZOGY algorithm (Zackay et al. 2016) to perform image subtraction on the NEOWISE images using the full-depth coadds of the WISE and NEOWISE mission (obtained during 2010–2014) as reference images. Photometric measurements were obtained

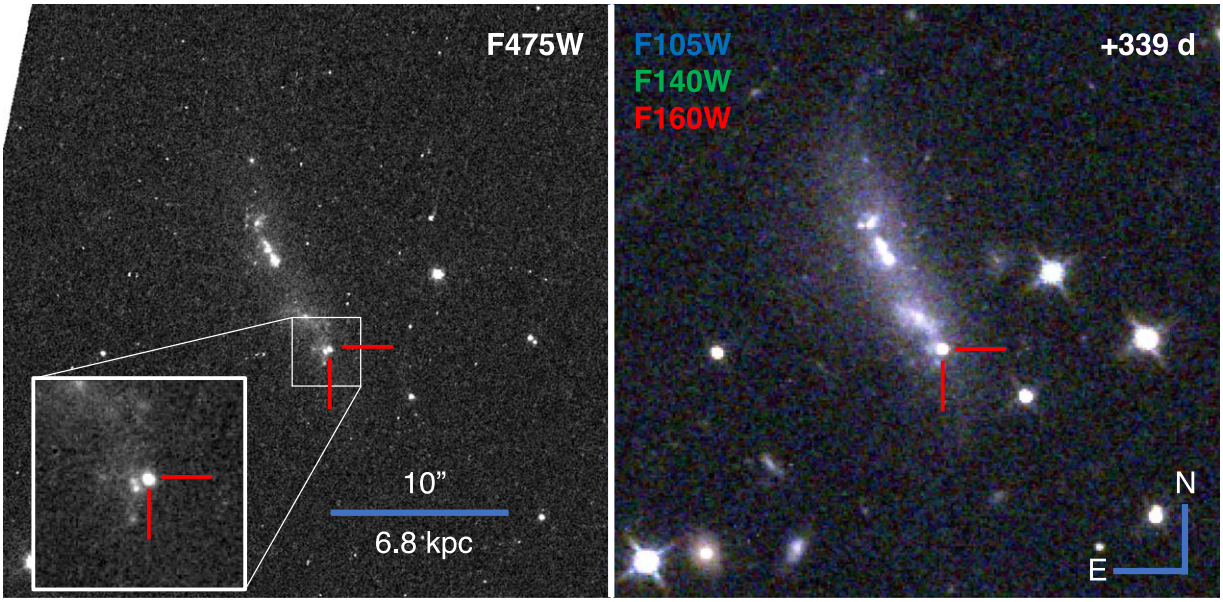

Figure 1. Images of SN 2020wnt at 339 days post peak taken by HST/WFC3 with the F475W filter (left, grayscale), and the F105W, F140W, and F160W filters (right, false color with the respective filters corresponding to blue, green, and red). The SN is marked with red crosses and the angular scale is notated. North is up and east is to the left. The inset of the left panel shows a zoomed-in image of the SN location. There are at least two neighboring sources to the SN, which are likely H II regions in the host galaxy.

by performing forced point-spread function photometry at the transient position on the subtracted WISE images until the epoch of the last NEOWISE data release (data acquired until 2021 December).

Lastly, we observed SN 2020wnt with the Wide-Field Camera 3 (WFC3) on board the Hubble Space Telescope (HST) in three epochs on 2021 December 15, 2022 January 25, and 2022 August 26 (GO–16768, PI: Tinyanont; SNAP–16691, PI: Foley). The first epoch consists of imaging with the F275W and F475W filters in the UVIS channel and the F105W, F140W, and F160W filters in the IR channel. The second epoch consists of shorter exposures with the F105W and F140W filters, along with spectroscopy with the G102 and G141 grisms. We will discuss the grism spectroscopy below. Figure 1 shows images of SN 2020wnt in different bands, while Figure 2 shows the light curves of SN 2020wnt.

The HST data presented in this article were obtained from the Mikulski Archive for Space Telescopes at the Space Telescope Science Institute. The specific observations analyzed can be accessed via doi:10.17909/hg36-3f30 (Tinyanont 2022).

2.3. Very Large Array Radio Observations

SN 2020wnt was observed with the Karl G. Jansky Very Large Array (VLA) under the Director's Discretionary Time program (program ID: 21B-161; PI: Yan). The observations were carried out on 2021 September 24 UT using the B-configuration for the *C* and *Ku* bands, each with a total of 42 minutes. The data were reduced using the standard procedures provided by the VLA software package Common Astronomy Software Applications (CASA; McMullin et al. 2007). SN 2020wnt is not detected in the cleaned maps, which reach 1σ rms of 5.4 and 6.5 μJy in the *C* and *Ku* bands, respectively.

2.4. Optical Spectroscopy

We obtained optical spectra of SN 2020wnt primarily with the Kast spectrograph (Miller & Stone 1993) on the 3 m Shane Telescope at Lick Observatory and the Low-Resolution Imaging Spectrograph (LRIS; Oke et al. 1995) on the Keck I telescope. The log of spectroscopic observations (both optical and near-IR in the next section) is provided in Table A1. Note that the last spectrum taken on 2022 September 22, 611 days post peak light, contains no discernible SN light; we use this spectrum with the longest exposure time for host analysis. The spectra were reduced using a custom data-reduction pipeline based on IRAF (Tody 1986).[20] The pipeline performed flat-field corrections using observations of a flat-field lamp. The wavelength solution was derived using observations of arc lamps. The instrument response function was derived using observations of spectroscopic standard stars. The two-dimensional spectra were extracted using the optimal extraction algorithm (Horne 1986).

We supplement this data set with spectra from the Alhambra Faint Object Spectrograph and Camera (ALFOSC) on the 2.56 m Nordic Optical Telescope (NOT) on La Palma and the Double Spectrograph (DBSP) at the 200 inch Hale Telescope at the Palomar Observatory (Oke & Gunn 1982). These data were reduced using similar steps as described above.

2.5. Infrared Spectroscopy

We obtained near-IR (1–2.5 μm) spectroscopy of SN 2020wnt at eight epochs, spanning −5 to 378 days from peak. We used the Near-Infrared Echellette Spectrometer (NIRES) on the Keck II telescope; TripleSpec (Herter et al. 2008) on the 200 inch Telescope at the Palomar Observatory; SpeX on IRTF; and the Gemini Near InfraRed Spectrograph (GNIRS; Elias et al. 2006a, 2006b) on the Gemini North telescope. NIRES and TripleSpec shared the same design and both provided a simultaneous wavelength coverage from 0.95 to 2.45 μm at $R \sim 2700$. They had $0\farcs55$ and $1\farcs0$ wide slits, respectively. The first epoch of SpeX

[20] The pipeline is publicly accessible at https://github.com/msiebert1/UCSC_spectral_pipeline.

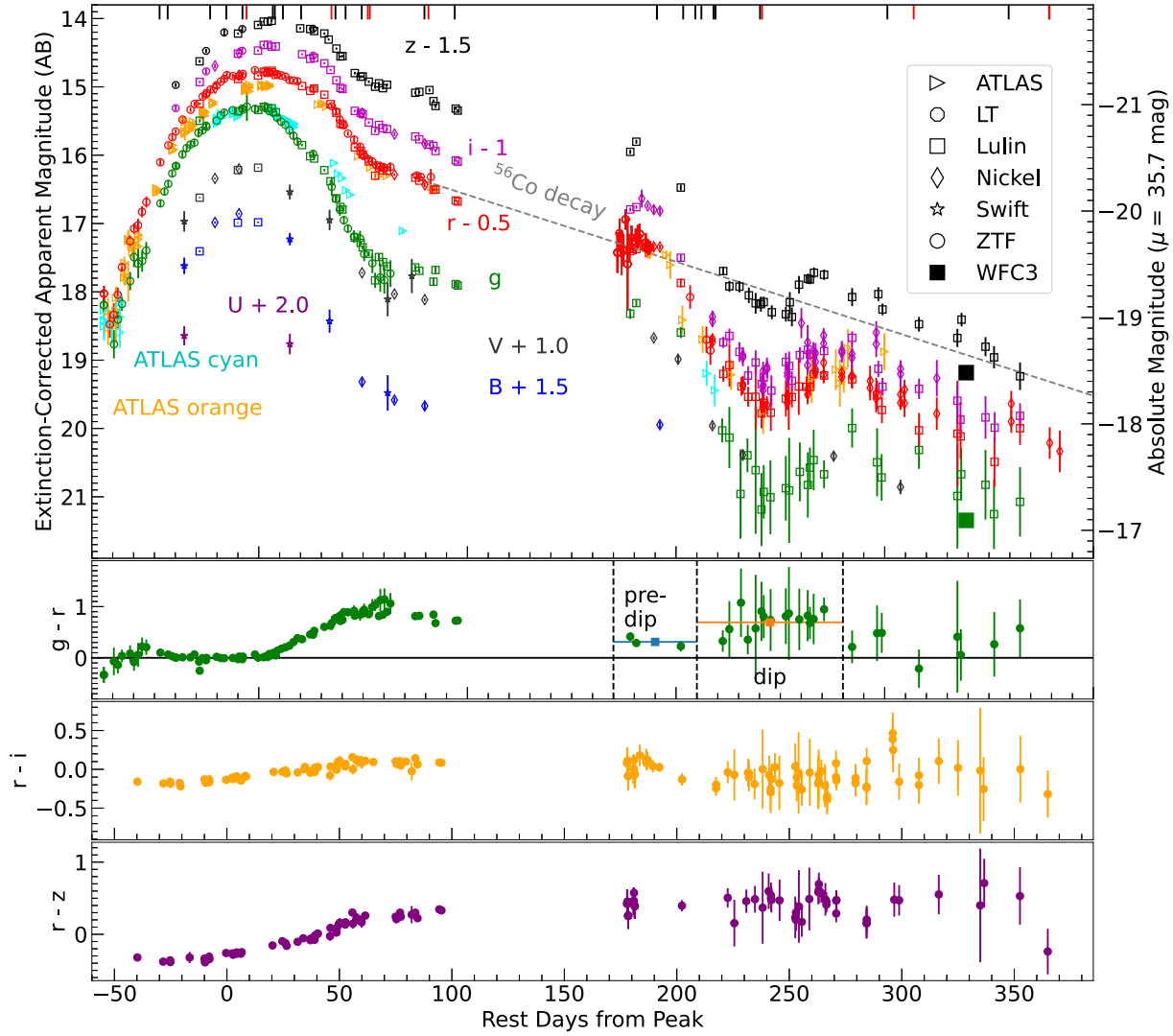

Figure 2. Top: multiband photometry of SN 2020wnt. All magnitudes are in the AB system (including the *UBV* bands). Different symbol shapes denote the telescope/instrument used. The two WFC3 photometry points plotted are in F475W (in green) and F110W (in black). The photometry has been corrected for Galactic extinction using $E(B-V) = 0.42$ mag and $R_V = 3.1$. Different bands are offset by the specified amount to improve visibility. The absolute magnitude is computed with a distance modulus of $\mu = 35.74$ mag. Black (red) ticks on top of the figure indicate the epochs with optical (near-IR) spectroscopy. The 0.0098 mag d^{-1} decline rate expected from the ^{56}Co decay is shown for comparison. Bottom: the evolution of $g-r$, $r-i$, and $r-z$ colors of SN 2020wnt. For the $g-r$ color, We mark the two regions around the light-curve dip and plot the average color pre-dip (170–210 days) and during dip (210–280 days). The multiband photometry is available as the data behind the figure.

(The data used to create this figure are available.)

observation was obtained as part of the program 2021A044 (PI: Tinyanont), using the short cross-dispersed mode paired with the 0.″8 wide slit, providing simultaneous wavelength coverage from 0.7 to 2.55 μm at a resolving power of $R \sim 750$. The second epoch, as part of 2021B058 (PI: Tinyanont), uses the low-resolution prism with the 0.″8 slit with a resolving power of $R \sim 70$. GNIRS data were obtained as part of the fast-turnaround programs GN-2021A-FT-104 and GN-2021B-FT-106 (PI: Tinyanont). We used the cross-dispersed mode with the short camera paired with the 32 l/mm grating and the 0.″45 wide slit, providing simultaneous wavelength coverage from 0.8 to 2.5 μm at a resolving power of $R \sim 1100$. At all epochs, we observed an A0V star for telluric corrections immediately before or after the science observations. We reduced the NIRES, TripleSpec, and SpeX data using `spextool` (Cushing et al. 2004), and the GNIRS data using the Gemini IRAF data-reduction package. We performed telluric corrections for all ground-based data using `xtellcor` (Vacca et al. 2003).

The last epoch of near-IR spectroscopy was performed using HST/WFC3 IR grisms G102 and G140. We obtained direct images in the F105W and F141W filters to provide the wavelength solution for the grism data based on the image position. We performed data reduction and spectral extraction using the package `HSTaXe`, following the official cookbook.[21]

All spectroscopic data will be made available through WISeREP[22] (Yaron & Gal-Yam 2012).

3. Light-curve Analysis

3.1. Bolometric Luminosity

We compute the bolometric luminosity of SN 2020wnt to capture the evolution of its radiative output using the following steps. We first interpolate the photometric data in different

[21] Accessed via https://github.com/npirzkal/aXe_WFC3_Cookbook.
[22] https://www.wiserep.org/

bands onto a common time grid using the Gaussian process regression package `george` (Ambikasaran et al. 2015) to perform the interpolation. We use the exponential squared kernel with a timescale of 500 days (we found that the result does not depend sensitively on the timescale). The interpolation is performed in the flux space. We do not use data extrapolated for more than 2 days from actual observations in further analyses.

With the interpolated light curve, we compute the bolometric light curve using `SuperBol` (Nicholl 2018), which fits a blackbody model reddened by the Milky Way dust extinction law ($R_V = 3.1$; Cardelli et al. 1989), with $E(B-V) = 0.42$ mag. We do not use any further interpolation in `SuperBol`. Most of our photometric follow-up observations begin after our spectroscopic classification at 43 days before peak; prior to that all photometric data come from ZTF and ATLAS. To avoid extrapolation, we run `SuperBol` for early-time ZTF and ATLAS photometry and for late-time photometry with more photometric bands separately. There is no jump in the resulting bolometric light curve. We find that suppressing flux at wavelengths shorter than 3000 Å to mimic the effects of line blanketing does not affect the results because there is already little flux at those wavelengths. For each epoch, `SuperBol` outputs the fitted blackbody temperature and radius. The bolometric luminosity is then the sum of the observed luminosity in all bands and the unobserved luminosity inferred from the blackbody fit. Figure 4 shows the resulting bolometric light curve of SN 2020wnt. It shows a comparison between the bolometric light curve of SN 2020wnt with that of typical slowly evolving SLSNe with well-observed light curves. We also plot the bolometric light curve of a typical, well-observed, normal SN Ic, 2007gr (Hunter et al. 2009), shifted by −1.5 mag. This comparison highlights that SN 2020wnt's light curve is more comparable both in peak luminosity and timescale to that of a slowly evolving SLSN than to a normal SN Ic.

We compute two peak epochs, in the r band and bolometric. In the r band, we find the peak at MJD = 59213, 75 days after the explosion. We use this peak epoch as a reference throughout the paper since it is less sensitive to uncertainties related to the bolometric fitting. From the bolometric light curve, we find the bolometric peak epoch and luminosity to be 69 ± 2 days post explosion in the rest frame and $L_{\rm bol,\,peak} = (6.8 \pm 0.3) \times 10^{43}\,{\rm erg\,s^{-1}}$ by fitting a low-order polynomial to the light curve around peak. This peak time is used to compute the SN explosion properties. The uncertainties are derived from a Markov Chain Monte Carlo (MCMC) fit performed using `emcee` (Foreman-Mackey et al. 2013). The total emitted energy as of our last epoch of observation is $\sim 5 \times 10^{50}$ erg.

At 585 days post peak, we derive a lower limit of the bolometric luminosity by running `SuperBol` on the two-band HST photometry. This is a lower limit because by this epoch the near-IR contribution to the emission is expected to be significantly larger than what is captured in the optical, and that the spectral energy distribution (SED) in the near-IR cannot be fit by extrapolating from the optical measurements. The SED also likely deviates significantly from a blackbody at this epoch. The SN is now too faint to observe in the near-IR with a ground-based telescope; space-based observations, especially with JWST, are required to measure the SED and the bolometric luminosity at this epoch. Thus, we mark this epoch with a triangle in Figure 9.

3.2. Light-curve and Color Evolution

We identify three phases of evolution of SN 2020wnt's light curve: an early shock-cooling phase, a symmetric peak, and a bumpy tail. Immediately after the explosion, both the ZTF and ATLAS data show a quickly fading emission with ∼5 days decline. Only a few epochs of data capture this feature. This is likely the cooling emission from the close-in CSM, or the extended progenitor envelope heated by the SN shock; it has been observed in a number of SLSNe I and SNe Ibc (e.g., Leloudas et al. 2012; Nicholl et al. 2015; Piro 2015; Smith et al. 2016; Taddia et al. 2016; Anderson et al. 2018; Angus et al. 2019; Gagliano et al. 2022). At this phase, the emission is blue with $g - r = -0.4 \pm 0.2$ mag (Figure 2, bottom).

After the initial shock-cooling emission, SN 2020wnt rises for 75 days, peaking first in the bluer bands. The color remains roughly constant in this phase with $g - r \sim -0.05$ mag. The SN reddens to $g - r = 0.8$ around 50 days post peak. The spectroscopic sequence, discussed in Section 4, will reveal that this color evolution is likely due to Fe-line blanketing.

After 50 days post peak, the light curve appears to settle on a linear magnitude decline. Figures 2 and 4 show that this initial slope is consistent with what is expected from a light curve powered by the radioactive decay of ^{56}Co. Starting at 100 days post peak, there is a 70 day gap in the coverage due to the solar conjunction. Afterward, the SN reemerges at magnitudes roughly expected from the radioactive decay model.

However, starting at ∼210 days post peak, the SN suddenly fades in all bands. This dip occurs between 210 and 280 days post peak, with the minimum at ∼240 days where the SN fades by about 1 mag. Figure 2 (bottom) shows that the SN also significantly reddens inside the dip, from the average $(g-r)_{\rm pre-dip} = 0.31 \pm 0.05$ mag before the dip (170–210 days) to $(g-r)_{\rm dip} = 0.69 \pm 0.05$ mag inside the dip (210–280 days). Note that the color scatter inside and after the dip is significant due to the faintness of the SN. The reported values here are weighted averages, and the error bars are standard errors of the mean. We discuss in Section 4.3 that this sudden dip and reddening of the light curve is likely due to dust formation and subsequent destruction.

3.3. Explosion Properties of SN 2020wnt Assuming Radioactivity

We first estimate the ejecta mass and ^{56}Ni mass of SN 2020wnt, assuming that the SN is powered solely by radioactivity. In the context of SLSNe I, this calculation typically shows that the ^{56}Ni mass needed to explain the luminosity is too large for the ejecta mass, thus requiring an additional power source.

We are using the analytic model of Khatami & Kasen (2019), which is an update of the classic Arnett (1982) model without the self-similarity assumption. This model produces results that are more in agreement with numerical simulations. In order to compute the ^{56}Ni mass, $M_{\rm Ni}$, produced in this SN, we use the peak luminosity of $L_{\rm peak} = (6.8 \pm 0.3) \times 10^{43}\,{\rm erg\,s^{-1}}$ derived previously. The peak epoch is $t_{\rm peak} = 69 \pm 2$ days post explosion in the rest frame. Since the rise time is much longer than the decay timescale of ^{56}Ni, we also consider the energy injection from the decay of ^{56}Co. The derivation in this scenario can be found in Appendix A1 in Khatami & Kasen (2019). We can rearrange their Equation

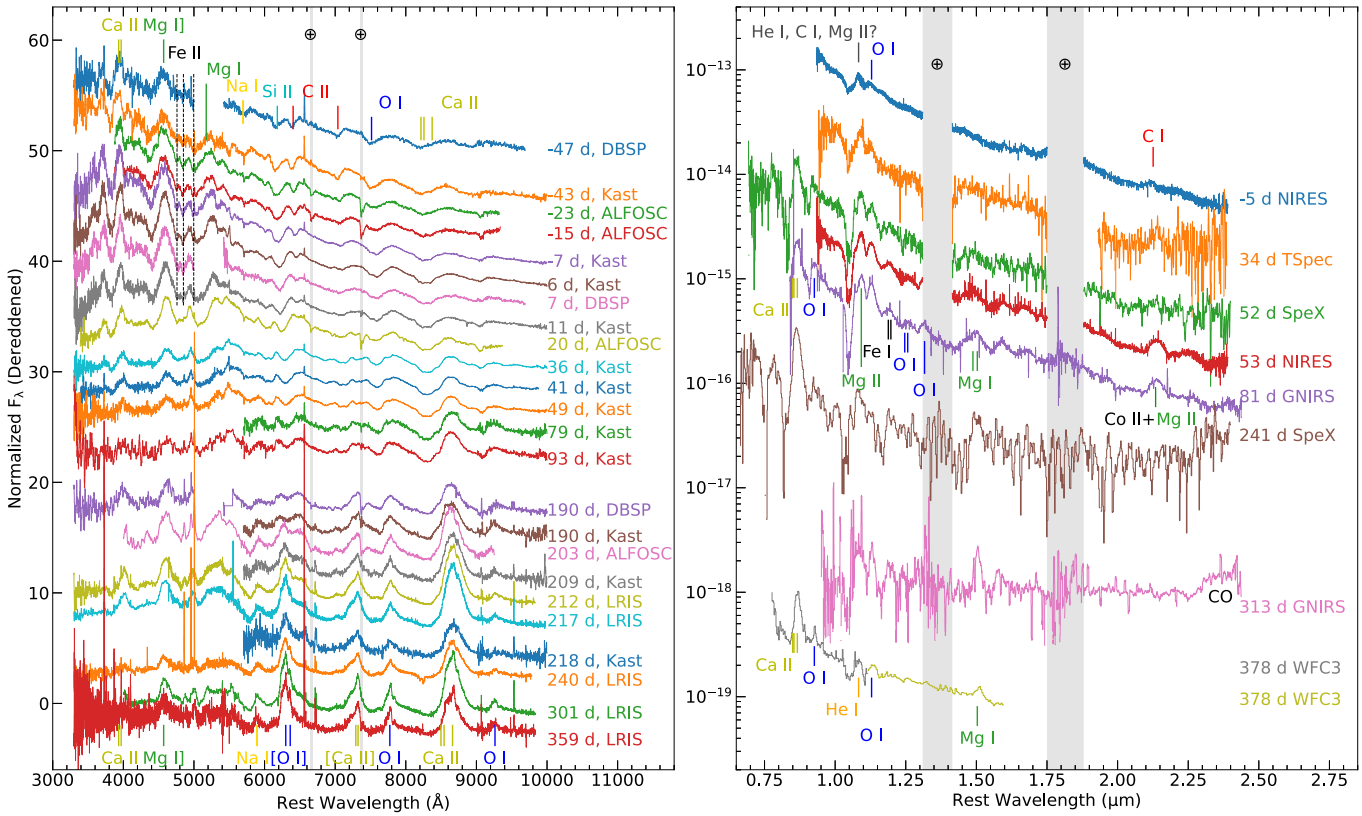

Figure 3. Optical (left) and near-IR (right) spectra of SN 2020wnt. The epoch of observation with respect to peak and the instrument used for each observation is notated. The near-IR spectra are plotted with a log scale on the *y*-axis to improve visibility. Spectra are also binned at varying resolutions for the same purpose. Prominent spectral features are marked. At early times, the Ca II H and K, Mg I], and Mg I lines are marked at rest showing the line peak; the Fe II lines are marked at $-10{,}000$ km s^{-1}; and the rest of the lines are marked at -8000 km s^{-1}, roughly corresponding to the P Cygni absorption minimum of each line. The emission lines at late times and all near-IR lines are marked at rest velocity. Telluric bands are also marked.

(41):

$$M_{\rm Ni} = L_{\rm peak}\frac{\beta^2\tau_{\rm Ni}^2}{2\epsilon_{Ni}}[0.83(1-\beta\tau_{\rm Ni})e^{-\beta\tau_{\rm Ni}} + 26.56(1-(1+\beta\tau_{\rm Co})e^{-\beta\tau_{\rm Co}})]^{-1}, \quad (1)$$

where β is a parameter describing the spatial distribution of the heating function and $\tau_{\rm Ni,\ Co} = t_{\rm peak}/t_{\rm Ni,\ Co}$. For ^{56}Ni and ^{56}Co, the decay timescales are $t_{\rm Ni} = 8.8$ days and $t_{\rm Co} = 111.3$ days, and the heating rates are $\epsilon_{\rm Ni} = 3.9\times10^{10}$ erg s^{-1} g^{-1} and $\epsilon_{\rm Co} = 6.8\times10^{9}$ erg s^{-1} g^{-1}, respectively. We obtain $M_{\rm Ni} = 7.3\pm0.2\,M_\odot$ for $\beta = 4/3$ (central heating source with constant opacity) and $M_{\rm Ni} = 5.6\pm0.2\,M_\odot$ for $\beta = 0.9$, appropriate for SNe Ic (Afsariardchi et al. 2021).

Next, we calculate the diffusion timescale using Equation (23) of Khatami & Kasen (2019). Here, we use the timescale of the ^{56}Co decay as the heating timescale, because this is the relevant decay for most of the rise: $t_s = 111.3$ days. Solving the equation, we obtain a diffusion timescale of $t_d = 114^{+4}_{-5}$ days. This quantity is related to the ejecta mass by rearranging (Khatami & Kasen 2019, their Equation (12)):

$$M_{\rm ej} = \frac{t_d^2 v_{\rm ej} c}{\kappa}, \quad (2)$$

where κ is the opacity, $v_{\rm ej}$ is the ejecta velocity, and c is the speed of light. For the ejecta velocity, we measure the absorption trough of the Fe II lines at 4924, 5018, and 5169 Å near peak light (Section 4), as these lines have been shown to probe the ejecta velocity in SNe Ic well (Liu et al. 2016; Modjaz et al. 2016) and have also been used in SLSNe I (Chen et al. 2023a). The velocity is $v_{\rm ej} = 10{,}300$ km s^{-1} (see Section 4.1). The electron scattering opacity in hydrogen-free ejecta at 11,000 K is $\sim$0.03 cm^2 g^{-1} (Khatami 2021, private communication). The ejecta mass calculated is $M_{\rm ej} = 52\pm2\,M_\odot(\kappa/0.03\,{\rm cm^2\,g^{-1}})$. Thus, the amount of ^{56}Ni required to power this SN is about 12% of the total ejecta mass, allowing the radioactive decay of ^{56}Ni and its daughter species to be the sole power source of this SN. We discuss in a later section that such a large amount of ^{56}Ni is very difficult to synthesize unless in a PISN, and that ultimately an additional power source is therefore still required to explain the luminosity of SN 2020wnt.

4. Spectroscopic Evolution

4.1. Optical Spectra

Figure 3 (left) shows the optical spectra of SN 2020wnt from -47 days to $+359$ days from peak light. The spectra lack hydrogen and helium at all epochs, and show features typical of SNe Ic. The most notable features at early times are the blueshifted absorption from C II at 6580 Å and 7231 Å. The 6580 Å absorption is comparable in strength to the Si II λ6350 before peak, and both C II features weaken as the SN evolves and disappear completely by about a month post peak. The velocity of the absorption minimum for both C II lines is -8000 km s^{-1} at 47 days before peak, and gets slower to about

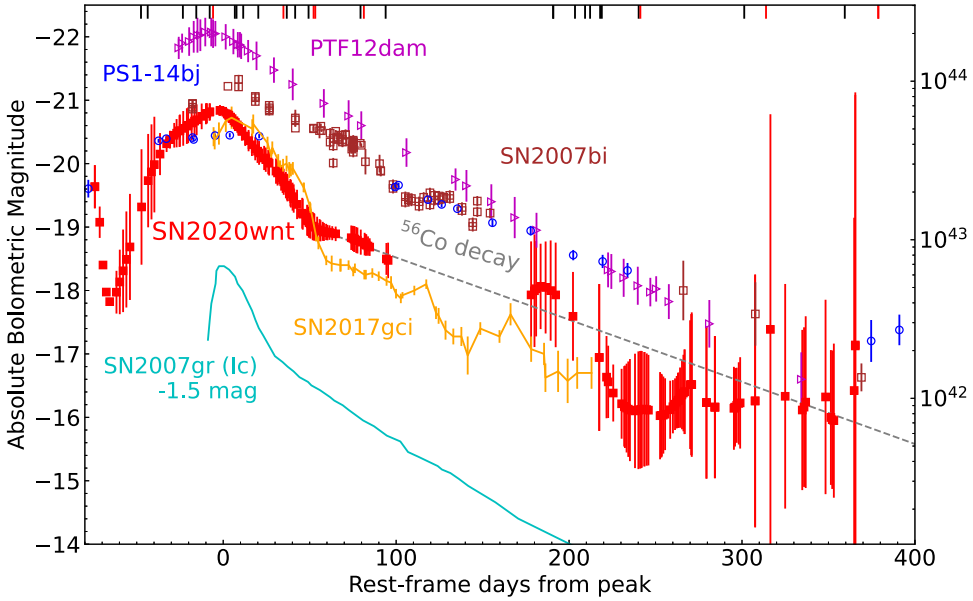

Figure 4. Bolometric light curve of SN 2020wnt compared with typical slowly evolving SLSNe (SN 2007bi, Gal-Yam et al. 2009; PTF12dam, Vreeswijk et al. 2017; PS1-14bj, Lunnan et al. 2016; SN 2017gci, Fiore et al. 2021) and a Type Ic (SN 2007gr, Hunter et al. 2009). These bolometric light curves are constructed in a similar manner, except for SN 2007bi, for which only r/R-band data exist. These comparison objects are well-observed representatives of their class. The knee in the light curve at 50 days post peak and the late-time decline rate make SN 2017gci the closest analog of SN 2020wnt. Black (red) ticks on top of the figure indicate the epochs with optical (near-IR) spectroscopy. The SN 2020wnt bolometric light curve is available as the data behind the figure. The data also includes the blackbody temperatures and radii.

(The data used to create this figure are available.)

-6000 km s^{-1} by 20 days post peak. The Si II λ6350 absorption also weakens and slows as the SN evolves, disappearing later at around 2 months post peak. In addition, strong features in early-time spectra include the Ca II H and K lines, the Na I D doublet (both broad lines intrinsic to the SN ejecta, as well as narrow interstellar absorption from the Milky Way), O I 7774 Å, and Ca II triplets. There is a persistent peak at 4571 Å, corresponding to the semi-forbidden Mg I], but at early times this feature could also be due to Fe-line blanketing on both sides. There are also persistent Fe II lines at 4924, 5018, and 5169 Å, which are shown to probe the ejecta velocity in SESNe (e.g., Branch et al. 2002; Bersten et al. 2012; Liu et al. 2016; Modjaz et al. 2016). Their velocity is consistently at $-10{,}300$ km s^{-1} until they disappear after peak. We adopt this as the ejecta velocity of SN 2020wnt (e.g., Section 3.3).

After peak luminosity, the blue part of the spectrum fades due to line blanketing from iron-group elements, reflecting the reddening observed in photometry. Other spectral features do not change significantly up to 93 days post peak, when the SN sets behind the Sun. The first spectra obtained after it reemerges $\sim$100 days later show that the absorption features are largely gone. Forbidden lines of [O I] 6300 and 6363 Å and [Ca II] 7292 and 7324 Å appear, indicating that the density in the ejecta has sufficiently decreased for these transitions to occur. Permitted lines from Na, O, and Ca previously seen in absorption are now in emission. We have one spectrum around the minimum of the light-curve dip at 240 days (Figure 4); we do not find significant spectral changes between this spectrum and those before and after the dip. We further discuss the spectroscopic evolution of SN 2020wnt in comparison with other SL and SESNe in a later subsection.

4.2. Near-infrared Spectra

Figure 3 (right) shows the near-IR spectra of SN 2020wnt from 5 days before to 378 days after peak light. The single near-IR spectrum prepeak (-5 days) is dominated by the thermal continuum with minimal spectral features. The line complex around 1.08 μm is present: this feature is potentially a blend between many lines, including He I 1.0830 μm, C I 1.0693 μm, Mg II 1.0927 μm, and S I 1.0457 μm (e.g., Shahbandeh et al. 2022). We do not detect the weaker He I 2.0581 μm line at any epoch. Other spectral features present at this epoch are the O I 1.1290 μm and the C I 2.1259 μm lines.

Between 52 and 81 days post peak, more spectral features emerge in the near-IR. Spectra with optical overlap (SpeX and GNIRS) show both the Ca triplet and the O I 9263 Å lines. The 1 μm line complex persists as well as the O I 1.1290 μm line. A number of peaks emerge throughout the near-IR wavelength range, resulting from multiple intermediate-mass and iron-group elements. We identify the peak around 1.19 μm from Fe I 1.1883, 1.1973 μm; the 1.257 and 1.3165 μm lines from O I (potentially with some contribution from the O I 1.2464 μm line); the 1.5 μm peak from Mg I 1.4878 and 1.5033 μm; and the 2.135 μm feature to be a blend between Co II 2.1347 μm and Mg II 2.1369 μm. Other features in the H band (e.g., at 1.59 and 1.68 μm) are likely due to iron-group elements.

After the solar conjunction, there are three spectra of SN 2020wnt obtained between 241 to 378 days post peak. The first spectrum, at 241 days, is from the low-resolution prism mode of SpeX, and the signal-to-noise (S/N) ratio is poor due to the faintness of the SN at this epoch ($K \approx 18.5$ mag). The second spectrum, with Gemini/GNIRS, has a better S/N. The last spectrum, from the HST/WFC3 IR grisms, has the best S/N of the late-time near-IR spectra, but it only covers out to 1.6 μm. No new spectral features from atomic species emerge

at this phase; however, the first overtone emission from CO is tentatively detected in the SpeX spectrum from 241 days, and is strongly detected in the GNIRS spectrum at 313 days. The thermal continuum also flattens in the red part of the spectra, in agreement with near-IR photometry obtained at similar epochs, suggesting dust formation (Figure 5). We discuss these features in more detail in Section 4.3.

The last spectrum we currently have from SN 2020wnt is obtained with the HST/WFC3 near-IR grisms at 390 days post peak. The continuum is still clearly present at this epoch and the strong 1 μm complex still has some P Cygni absorption. We note, regardless, that the peak of the 1 μm complex is now at the rest velocity of He I. A later observation will allow us to more confidently identify the species responsible for the 1 μm complex. We further compare this spectrum to models of massive core-collapse SNe and PISNe in Section 7.2.

4.3. Formation of Carbon Monoxide and Dust

SN ejecta form molecules as they expand and cool, starting with simple molecules and progressing to more complex molecules and dust grains as the temperature drops. Dust formation in SN ejecta is of particular interest because it has the potential to explain the large dust mass observed in the early universe (e.g., Gall et al. 2011 and references therein), before other dust-forming objects such as asymptotic giant branch (AGB) stars had sufficient time to evolve. While massive stars may produce dust in their outflows (e.g., Lau et al. 2021), their death as CCSNe is potentially the dominant channel (e.g., Gall & Hjorth 2018). Various observations of SN 1987A and SN remnants in the radio and submillimeter demonstrate that $\sim$0.1 $M_\odot$ of dust can eventually form in the aftermath of a CCSN (e.g., Rho et al. 2008, 2009; Barlow et al. 2010; Indebetouw et al. 2014; Dwek & Arendt 2015; Lau et al. 2015; Matsuura et al. 2015; Rho et al. 2018b). However, measurements from near- to mid-IR photometry and spectroscopy of CCSNe from months to years post explosion (e.g., Szalai & Vinkó 2013; Tinyanont et al. 2016; Szalai et al. 2019; Tinyanont et al. 2019; Rho et al. 2021; Li et al. 2022) show that the mass of newly formed dust at these early times remain modest, at around 10^{-5}–$10^{-3}\,M_\odot$. (Strongly interacting SNe show much larger dust mass, but most of it is likely preexisting in the CSM; Fox et al. 2011, 2013.) In the coming years, JWST near-to-mid-IR spectroscopy will paint a much more complete picture of the evolution of dust mass in local CCSNe. However, a question remains whether primordial CCSNe with massive progenitors and small metallicity produce molecules and dust in the same way.

Prior to dust formation, SN ejecta form more simple molecules since these less complex chemical species can withstand higher temperature and pressure. CO is the first molecule to form due to its strong molecular triple bond. In SN 2020wnt, the first sign of CO emerges around 230 days post peak (around 300 days post explosion). The near-IR spectrum from 241 days shows a tentative detection of the first overtone band of CO starting at 2.3 μm, a feature which strengthens and is clearly detected at 313 days (Figure 5). Further, the WISE photometry from 233 days shows a strong excess in the W2 (4.6 μm) channel, which is centered on the CO fundamental band.

CO emission has been observed in CCSNe of all types with late-time near-IR spectra (e.g., Spyromilio et al. 1988; Gerardy et al. 2002; Rho et al. 2018a; Davis et al. 2019; Tinyanont et al. 2019; Rho et al. 2021; Shahbandeh et al. 2022). The formation happens in the C/O rich layer (helium-burning product) of the ejecta (Sarangi & Cherchneff 2015; Jerkstrand et al. 2017), equally depleting carbon and oxygen from the gas, leaving the remaining elements for further dust formation. Carbon-rich materials can form different forms of carbonaceous dust such as amorphous carbon and graphite. Oxygen-rich materials further form oxides such as SiO and SiO_2, and eventually silicate dust. Other oxygen-rich molecules, e.g., CO_2 and O_2, may eventually form as well. CO emission also cools the ejecta to temperatures appropriate for dust formation ($\lesssim$1500 K; Sarangi et al. 2018 and references therein). Detecting this feature in the majority of SLSNe is impossible from the ground because the 2.3 μm band head gets redshifted out of the ground-based near-IR band ($\sim$2.5 μm) at a redshift of only $z = 0.087$. The CO detection in SN 2020wnt presents a strong case for near- to mid-IR observations of SLSNe with JWST to start to map the chemical evolution in the ejecta of these explosions.

In addition to the CO emission, we detected a rising continuum, as seen in Figure 5, presumably from dust grains. During the strong light-curve dip around 220 days post peak,

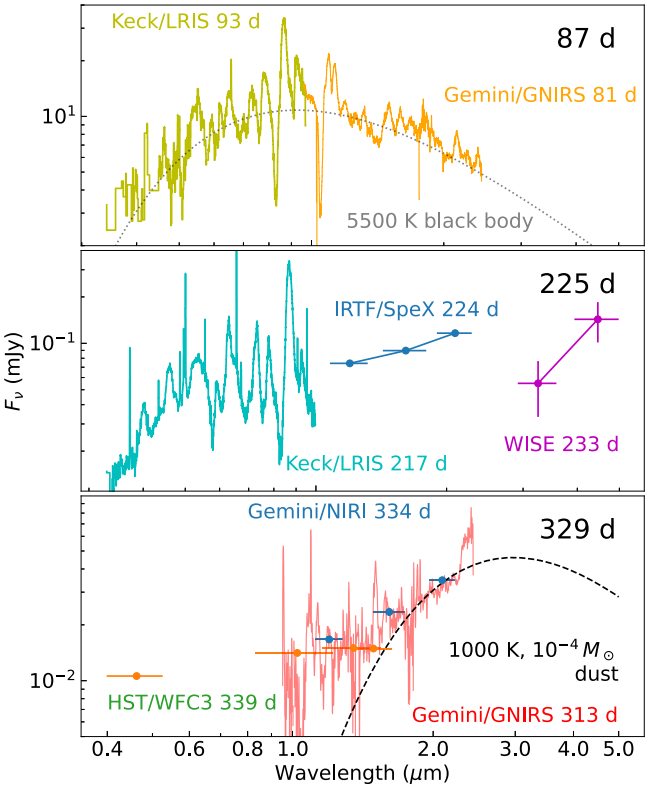

Figure 5. Evolution of the SED of SN 2020wnt. Multiband photometry and spectroscopy from three epochs, 87, 225, and 329 days post peak, are shown in the top, middle, and bottom panels, respectively. The data are corrected for the Galactic extinction. At $\sim$87 days, the SED can be explained as 5500 K blackbody radiation. At 217–233 days, the near-IR contribution becomes significant, and there is a sign of CO formation in the W2 channel of WISE. The data from different epochs in this panel are scaled based on the *r*-band photometry because this is the epoch during which the light curve declines quickly. We note that the fluxes from SpeX and WISE do not match up, likely because the SN was quickly fading around this epoch. The near-IR contribution strengthened, and by $\sim$329 days a continuum from hot, 1000 K dust is needed to explain the SED. The inferred dust mass, assuming a simplistic 0.1 μm carbonaceous grain population, is $10^{-4}\,M_\odot$. The first overtone emission of CO is also clearly detected around 2.3 μm.

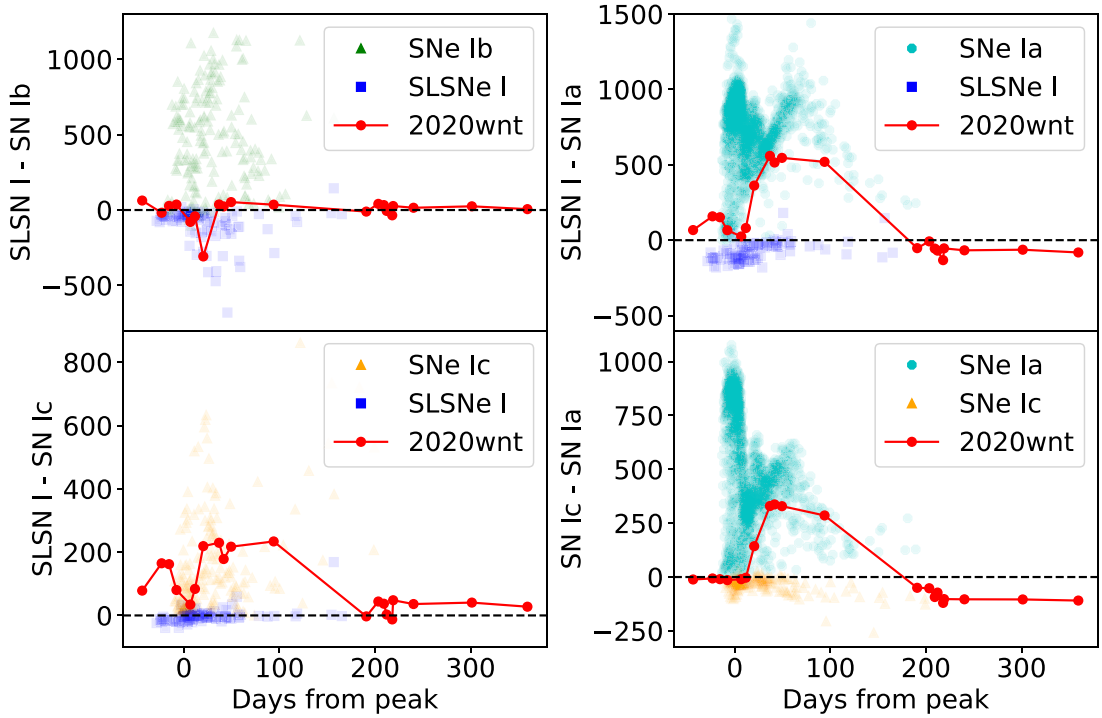

Figure 6. Classification score differences of SN 2020wnt, in comparison with other SNe and SLSNe in the literature. The literature data come from Quimby et al. (2018), and these plots resemble their Figures 3 and 4. Clockwise, starting from top left, we plot the SLSN I−Ib, SLSN I−Ia, Ic−Ia, and SLSN I−Ic scores. These scores allow us to quantitatively determine if a given spectrum more resembles one class or another in a pairwise fashion. For instance, in the SLSN I−Ib plot, most known SNe Ib have positive score difference while SLSNe I are negative. SN 2020wnt's spectra lie close to zero, meaning that both classes are unlikely. From these plots, we can conclude that the spectra of SN 2020wnt resemble those of SNe Ic at all phases, and also SNe Ia at around 1 month post peak. We provide further discussion in the text. The classification score differences for SN 2020wnt are available as the data behind the figure.

(The data used to create this figure are available.)

the SED with near-IR photometry from SpeX and WISE shows an emerging dust thermal continuum (though the W2 point is likely contaminated by CO emission). At around 330 days post peak, the SED can be explained by adding a thermal component of hot dust with $T = 1000$ K and $M = 10^{-4}\,M_{\odot}$, assuming a simple population of 0.1 μm carbonaceous grains. This dust mass is comparable to what was observed in SN 2018bsz (Chen et al. 2021). However, we note that their observations were photometric at 3.6 and 4.5 μm, and that their dust models peak at around 6 μm, inferring a dust temperature of around 500 K. If we were to infer our dust mass based on the WISE observations (Figure 5), the results could be biased by the CO emission in the 4.5 μm band. The available data are insufficient to distinguish different dust compositions and grain sizes; mid-IR spectroscopy covering the silicate features at 10 and 18.9 μm is needed.

To determine whether dust formation explains the sudden reddening and decline in the luminosity at around 210 days post peak, we compute the time-dependent reddening of SN 2020wnt by fitting its SED around the dip, assuming a constant temperature of 8000 K, the temperature found by `SuperBol` for this epoch. Note that this temperature was derived assuming the Galactic extinction with $E(B-V) = 0.42$. The extra time-dependent extinction found by this analysis is assumed to be intrinsic to the SN.

During the dip, the maximum total reddening is $E(B-V) \approx 0.69$ mag, corresponding to $A_r = 1.7$ mag (an increase from $A_r = 1.0$ mag just from the Milky Way). The decrease in r-band flux during the dip compared to the interpolated light curve from pre- and post-dip photometry is 1.84 mag, suggesting that dust formation can roughly account for the flux decrement at these times. To explain the recovery out of the dip later, the dust can be destroyed by the shock front or there is a strong asymmetry in dust formation which allows the dusty part of the ejecta to obstruct a smaller solid angle at later times.

Molecule and dust production in SNe remain poorly constrained due to the lack of IR observations. For SLSNe I, there has only been one event with signs of dust formation detected with Spitzer (SN 2018bsz; Chen et al. 2021), and three more with WISE (Sun et al. 2022). For SN 2018bsz, CSM interactions, which resulted in a strong Hα emission, not seen in SN 2020wnt, may have played a role in illuminating preexisting dust or forming new dust in the post-shock ejecta (Pursiainen et al. 2022). SN 2020wnt shows that the dust continuum could also be present in an event with no strong signatures of interactions. In addition to the similar dust formation signature, SN 2018bsz also showed C II in early-time spectra, similar to SN 2020wnt. However, it has a very different photometric evolution and shows O II absorption and a blue continuum, typical SLSNe I features (Anderson et al. 2018; Chen et al. 2021; Pursiainen et al. 2022). With model predictions of continued dust formations in these SLSN remnants aided by the pulsar emission from the magnetar (Omand et al. 2019), and the possibility that these superluminous explosions are more common in the early universe, further space-based IR observations are warranted.

4.4. Optical Spectral Similarities to Stripped-envelope Supernovae near Peak

To quantitatively show that SN 2020wnt is spectroscopically more similar to SESNe (and to an extent SNe Ia) near peak than to engine-driven SLSNe, we follow the methodology outlined in Quimby et al. (2018) to quantitatively determine a spectrum's classification. We compare the optical spectra of SN 2020wnt to a large template library of SN spectra from Quimby et al. (2018) [23] using `Superfit` (Howell et al. 2006). We similarly limit the wavelength range used to 3900–7000 Å, to avoid biases due to the incomplete wavelength coverage of many of the templates. We do not perform this analysis on our spectra with a gap in this wavelength region for the same reason. We limit the redshift range searched by `Superfit` to keep the runtime reasonable. All other setups are the default. Given an observed spectrum, `Superfit` provides a list of best-match templates ranked inversely by the χ^2 value of the fit. We then compute a classification score for each class by averaging the indices of the top five matches for each class. For instance, if the first five SLSN I templates that match a given spectrum have indices 0, 1, 3, 5, and 6, the SLSN I classification score for this spectrum is 3. The class with the smallest score is thus the best match.

Quimby et al. (2018) showed that the difference between classification scores of two classes (e.g., SN Ic—SLSN I) can reliably distinguish SLSNe from other types of SNe (and also different SNe subtypes from each other). This result establishes that SLSNe form a distinct spectroscopic class from other SESNe, regardless of the luminosity, and that some SLSNe peak at lower luminosities than the traditional cutoff at −21 mag.

Figure 6 shows the SLSN I−SN Ia, Ib, Ic, and SN Ia−Ic scores of SN 2020wnt, plotted on top of other SNe of known subtype from Quimby et al. (2018). The left column shows the SLSN I−SN Ib and Ic scores, while the right column shows the SLSN I−SN Ia and SN Ic−Ia scores. These plots demonstrate that the score differences reliably distinguish SNe with different known spectral types. SN 2020wnt lies roughly on the zero line for the SLSN I−SN Ib score, showing that it unlikely belongs to either class. The SLSN I−SN Ia and Ic plots show that SN 2020wnt better resembles either SNe Ia or Ic than it does SLSNe I. Lastly, in the SN Ic−Ia plot, SN 2020wnt better resembles SNe Ic at most epochs, except for the epochs between 20 and 93 days post peak. These plots also show that the spectra with most distinguishing power (largest score differences) are those from between 30 and 100 days post peak, around the time when SN 2020wnt enters the nebular phase, revealing its inner ejecta. After around this phase, the analysis becomes difficult due to the lack of template spectra at these epochs.

To visualize this similarity, Figure 7 shows select high-S/N spectra of SN 2020wnt prepeak (−43 days), near peak (+6 days), in its early nebular phase (49 days), and later in the nebular phase (+359 days), in comparison with SN 2007gr (SN Ic; Valenti et al. 2008; Hunter et al. 2009), SN 2015bn (SLSN I; Nicholl et al. 2016a, 2016b), and SN 2017gci (SLSN I; Fiore et al. 2021) at comparable epochs. These objects are chosen to be representative of their respective classes that are very well observed. We include the mean nebular SLSN and SN Ic spectra from Nicholl et al. (2019) at late time, in order to discuss SN 2020wnt in context of other SLSNe and SNe Ic. We also include a spectrum of SN Ia (91T-like) 1999dq (Blondin et al. 2012) at 29 days post peak, which is the best match to the early nebular spectra of SN 2020wnt. This spectrum is similar to that of a normal SN Ia at this phase.

The prepeak spectra (top two panels in Figure 7) clearly show the lack of both a hot continuum and a series of O II absorption, which are associated with SLSNe I. The ejecta of SLSNe I get continuously heated by the central magnetar, allowing them to remain hot and producing these spectral features all the way from explosion to even after peak light (Nicholl 2021 and references therein). The absence of this temperature excess in SN 2020wnt requires that a central engine either does not exist or that its effects are concealed until well after peak.

At around 50 days post peak, when the light curve of SN 2020wnt falls onto the approximately linear decline, the spectra are best matched not by SNe Ic, but SNe Ia. The lower-right panel of Figure 6 and the middle panel (third from top) of Figure 7 show that while the spectrum of SN 2020wnt remains distinct from those of SLSNe I, it now more resembles that of a SN Ia, rather than a SN Ic at a comparable phase. In fact, during this phase the first SN Ic match we obtain from `Superfit` is number 320 on the list; everything above is a SN Ia spectrum. This result suggests that the composition of the outer ejecta of SN 2020wnt and the temperature (thus atomic excitation states) are similar to those of SNe Ia at this epoch. Detailed modeling of this phase of spectra is beyond the scope of this paper.

4.5. Late Nebular Spectra Reveal a Magnetar

Nicholl et al. (2019) compared nebular spectra of SLSNe I and SNe Ic and demonstrated that, while they are less distinguishable than spectra near peak, there are a number of subtle differences between nebular spectra of SLSNe I and SNe Ic, potentially due to magnetar heating in the former class. First, the mean nebular spectrum of SLSNe I has more luminous recombination O I 7774 Å emission with a relatively narrow profile, indicating that it originates in the inner ejecta. This line demonstrates that the inner ejecta of SLSNe I remain ionized at late times due to the power-law nature of magnetar heating luminosity (as opposed to exponential decay for radioactivity). Second, the mean nebular spectrum of SLSNe I shows an emission feature at 5000 Å, which Nicholl et al. (2019) identified as [Fe II] and [O III]; a magnetar is again required to keep the inner ejecta at such a high ionization state at late times. Third, SLSNe I show elevated flux in the blue part of the spectrum, due to a large iron-group element synthesized in the magnetar-driven explosion. This blue pseudo-continuum is similar to what is observed in SNe Ic-BL, like SN 1998bw, which are known to produce a relatively large amount of iron-group elements (0.3–0.7 $M_\odot$ in the case of SN 1998bw; Galama et al. 1998; Sollerman et al. 2002). The bottom panel of Figure 7 compares the last optical spectrum of SN 2020wnt with the mean late-time spectra of SLSNe I and SNe Ic, both from Nicholl et al. (2019). The late nebular spectrum of SN 2020wnt shows all these three features, and much more closely resembles the mean SLSN I spectrum.

From these spectra, we conclude that SN 2020wnt harbors a magnetar. However, unlike in other SLSNe, the magnetar is hidden inside the optically thick ejecta near peak, and does not imprint perceptible spectroscopic signatures. This finding is quite similar to the case of iPTF15dtg, whose peak spectra

[23] Accessible at https://github.com/rmquimby/2018ApJ...855....2Q.

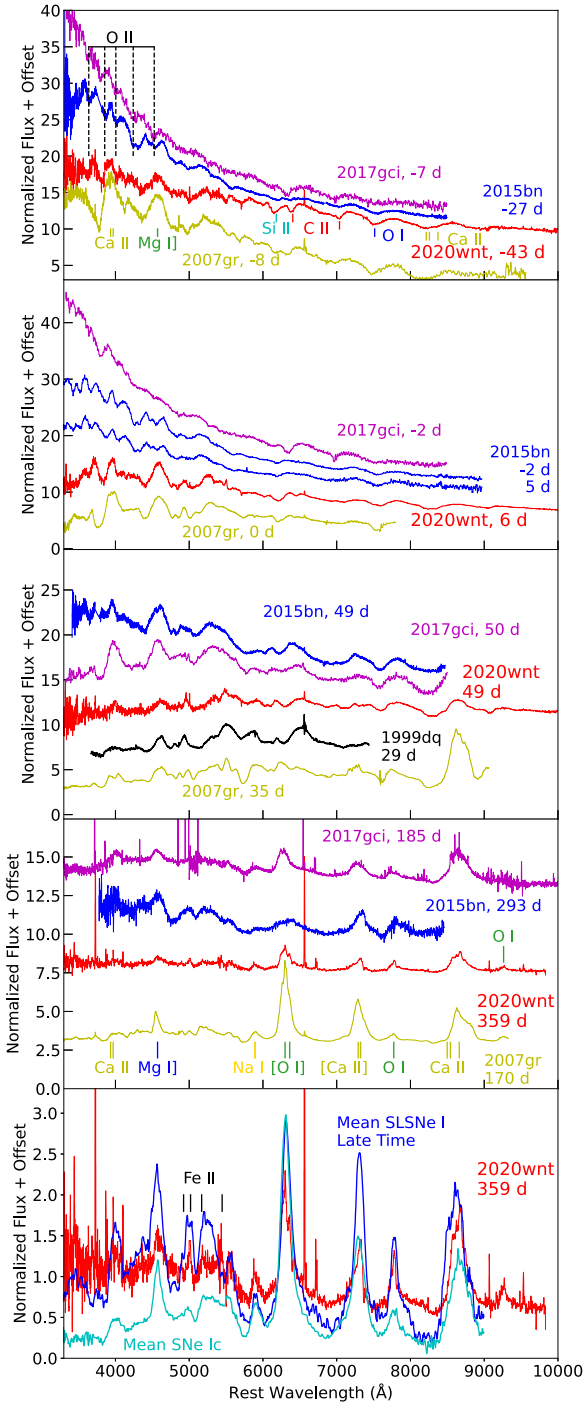

Figure 7. Top four panels: optical spectra of SN 2020wnt at −43, 6, 49, and 359 days from peak, compared with those of SN Ic 2007gr (Hunter et al. 2009); and SLSNe 2015bn (Nicholl et al. 2016a, 2016b), and 2017gci (Fiore et al. 2021) at comparable epochs. For the 49 days epoch, the best-matched spectrum, SN 1999dq (Ia 91T-like; Blondin et al. 2012) from 29 days post peak, is also shown. Bottom: the last optical spectrum of SN 2020wnt at 359 days compared with the mean late-time SLSN I and SN Ic spectra from Nicholl et al. (2019). The two mean spectra plotted are similar to their Figure 8. We mark select Fe II lines from the model spectra of Dessart (2019) that are detected in SN 2020wnt.

clearly resemble those of normal SNe Ic (Taddia et al. 2016) but late-time observations show signs of magnetar power (Taddia et al. 2019) in both the light-curve evolution and the optical spectra. The implication here is that we may not be able

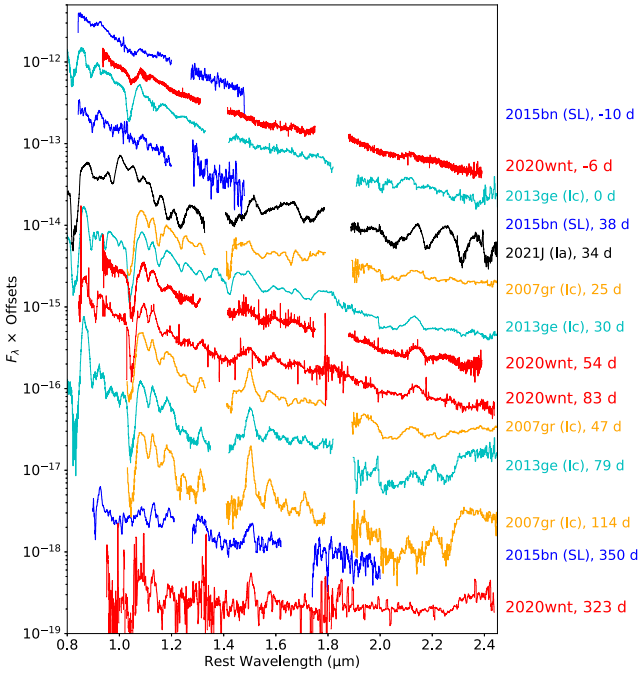

Figure 8. Comparison between near-IR spectra of SN 2020wnt at −6, 54, 83, and 323 days from peak and spectra of SNe Ic 2007gr (Hunter et al. 2009) and 2013ge (Shahbandeh et al. 2022), SLSN 2015bn (Nicholl et al. 2016a; Jerkstrand et al. 2017), and SN Ia 2021J from our IRTF observations. Spectra of other SNe are provided at comparable epochs provided availability.

to use peak-time spectra alone to select magnetar-driven explosions from a population of hydrogen-poor CCSNe. In some cases, like SN 2020wnt, spectroscopic signatures of the magnetar are not apparent until ∼a year post peak. A survey of nebular spectra of SESNe is needed to determine the fraction of these explosions significantly powered by a central engine.

4.6. Near-infrared Spectral Comparison

Figure 8 compares the near-IR spectra of SN 2020wnt at −6, 54, 83, and 323 days from peak with the spectra of SNe Ic 2007gr (Hunter et al. 2009) and 2013ge (Shahbandeh et al. 2022), SLSN 2015bn (Nicholl et al. 2016a), and SN Ia 2021J about 1 month post peak (this work). SN 2013ge is added for comparison because it is a SN Ic with the most epochs of near-IR spectra taken by the Carnegie Supernova Project II (Hsiao et al. 2019; Shahbandeh et al. 2022), clearly showing the formation of CO. SN 2021J is added as a representative SN Ia for which we have a near-IR spectrum at around 1 month post peak. These are comparable in epoch to the optical comparison in Figure 7. In the near-IR, SN 2020wnt spectra also better resemble those of SNe Ic compared with those of SLSNe I, especially around 40–50 days post peak, where SN 2020wnt and SNe Ic have a strong P Cygni absorption at 1 μm, a feature that is missing in SN 2015bn. The comparison is more difficult because there are only a handful of SNe Ic with multiepoch near-IR spectra and there are only a few near-IR spectra of any SLSNe I (e.g., Gaia16apd, Yan et al. 2017b; LSQ14an, Jerkstrand et al. 2017). Note that the spectra of SN 2015bn have smaller wavelength coverage due to the significant redshift and the lack of *K*-band observations in the first two epochs. Its ground-based spectra never cover the CO band head, despite the

relatively modest redshift for a SLSN, highlighting the need for JWST to discern molecule (and dust) formation in SLSNe.

The most notable difference between the near-IR spectra of SLSNe and those of SNe Ic and SN 2020wnt is the 1 μm complex. The spectra of SN 2015bn lack the deep P Cygni absorption from this spectral feature at all epochs. This difference is most stark when comparing the SN 2015bn spectrum from 350 days post peak and that of SN 2020wnt 323 days post peak. While the peak at 1.08 μm (likely due to He I at these epochs), the O I 1.1290 μm line, and the Mg I 1.5033 μm line are present in both spectra, the deep P Cygni absorption associated with the 1.08 μm feature, observed in SN 2020wnt at all epochs, is missing from the spectra of SN 2015bn. The presence of the P Cygni feature here also suggests that the ejecta of SN 2020wnt are more optically thick than those of SLSNe, even at this late phase. The P Cygni absorption is not obviously present in any other lines in the optical at this epoch, likely due to the weaker continuum or the abundance of lines.

Lastly, while the nebular spectra of SN 2020wnt from about 50–100 days post peak resemble those of SNe Ia from about 20 to 30 days post peak, the near-IR spectra are completely different. We show an IRTF spectrum of SN 2021J at 34 days post peak, which has completely different spectral features compared to SN 2020wnt and SNe Ic. (This spectrum was obtained with IRTF/SpeX with the same observation and data-reduction details as those for the SN 2020wnt's SpeX spectra.) Most features are due to iron-group elements, which are abundant and are the main coolants in SNe Ia. The lack of these features in SN 2020wnt does not necessarily imply a small amount of iron-group elements; indeed, PISN nebular spectral models, e.g., Jerkstrand et al.'s (2016) and Mazzali et al.'s (2019), all show modest iron-group emissions in the near-IR despite the large amount of iron-group elements synthesized in those explosions. With its massive ejecta, the iron/nickel-rich part may still be embedded at these early nebular epochs. Even at later times when the inner ejecta are visible, the primary coolant could still be other atomic and molecular lines. Further detailed modeling of the IR spectra is needed to constrain the amount of iron-group elements from the ejecta.

5. Radio Limit on Circumstellar Medium Density

Radio observations of SN 2020wnt at 335 days post explosion, 260 days post peak allow us to place a limit on the wind density around the progenitor star. Note that this limit only applies to the wind density around the shock location at the epoch of observations; it does not preclude a dense CSM close to the SN. Because of the lack of narrow lines from the ionized CSM in any phase, we assume that the radio absorption is dominated by synchrotron self-absorption, and not free–free absorption in the CSM. We use Equation (12) in Chandra (2018; Equation (14) in Chevalier 1998) to convert the observed flux limits to upper limits on the magnetic field in the shock front of SN 2020wnt:

$$B = 0.58 a^{\frac{-4}{19}} \left(\frac{f}{0.5}\right)^{\frac{-4}{19}} \left(\frac{F_{\rm peak}}{\rm Jy}\right)^{\frac{-2}{19}} \left(\frac{d}{\rm Mpc}\right)^{\frac{-4}{19}} \left(\frac{\nu_{\rm peak}}{5\ {\rm GHz}}\right) {\rm G}, \quad (3)$$

where $a = \epsilon_e/\epsilon_B$ is the equipartition parameter (ratio between the shock energy deposited in relativistic electrons and magnetic field), f is the volume filling factor of the CSM, and $F_{\rm peak}$ and $\nu_{\rm peak}$ are the flux and the frequency of the peak in the radio SED. This formula assumes the power index of the electron energy distribution, $N(E) \propto E^{-p}$, to be $p = 3$. Equating the magnetic pressure to the shock ram pressure, $B^2/8\pi = \zeta \rho_{\rm wind} v_{\rm shock}^2$, where $\zeta < 1$ is a numerical factor, one can derive Equation (13) in Chandra (2018):

$$\dot{M} = \frac{6 \times 10^{-7}\ M_\odot\ {\rm yr}^{-1}}{m^2 \zeta} \left(\frac{B}{1\ {\rm G}}\right)^2 \times \left(\frac{t}{100\ {\rm days}}\right)^2 \left(\frac{v_{\rm wind}}{10\ {\rm km\ s^{-1}}}\right), \quad (4)$$

where m is the deceleration factor, which we assume to be 1 (constant velocity shock). We rearrange this in terms of $\dot{M}/v_{\rm wind}$, the wind density parameter, since we have no constraint on the wind velocity:

$$\frac{\dot{M}}{v_{\rm wind}} = \frac{3.8 \times 10^{13}\ {\rm g\ cm^{-1}}}{m^2 \zeta} \left(\frac{B}{1\ {\rm G}}\right)^2 \left(\frac{t}{100\ {\rm days}}\right)^2. \quad (5)$$

From these equations, we note that the magnetic field, and thus the wind density parameter, only depends weakly on the observed radio flux. What sets the limit is the break frequency of the radio SED, $\nu_{\rm peak}$. For SN 2020wnt, there is no detection at 335 days post explosion, so we use the flux upper limit at the lowest observed frequency to put a constraint on the wind parameter of its CSM. This is $F_{\rm peak} < 5.4$ μJy in the C band, at 5 GHz. Because of the also deep nondetection (<6.5 μJy) in the Ku band, at 15 GHz, we assume that $\nu_{\rm peak} < 5$ GHz. While the peak frequency could be much higher and the emission is completely self-absorbed at our observed frequency, the CSM density would be high, which is inconsistent with the lack of narrow lines in the optical at any epoch. While a compact and dense CSM can exist at early times within the photosphere and not showing any narrow lines, such a CSM would be revealed later. This is not the case in SN 2020wnt. Thus, the high CSM density scenario is unlikely at the epoch of observation.

We thus get an upper limit on the magnetic field of $B < 0.63$ G, and the wind density parameter of $\dot{M}/v_{\rm wind} < 1.7 \times 10^{14}$ g cm^{-1}, or $\dot{M} < 1.3 \times 10^{-4}\ M_\odot\ {\rm yr}^{-1} (v_{\rm wind}/500\ {\rm km\ s^{-1}})$. This upper limit rules out dense and extended CSM seen in strongly interacting SNe, which have $\dot{M}/v_{\rm wind} \gtrsim 5 \times 10^{15}$ g cm^{-1} (Smith 2017), and is consistent with the progenitor of SN 2020wnt being a massive stripped star.

From this wind density parameter limit, we can also calculate a limit on the total luminosity from CSM interactions: $L_{\rm CSM} \sim 1/2\ \dot{M} v_{\rm wind} v_{\rm shock}^3$. With a shock velocity between 10,000 km s^{-1} (ejecta velocity from the Fe II) and 20,000 km s^{-1} (velocity of the outer shock from the lowest-mass explosion model in Section 6), the interaction luminosity ranges from 9×10^{40}–7×10^{41} erg s^{-1}. At the brightest, the interaction luminosity does not significantly contribute to the bolometric luminosity of SN 2020wnt until at least 500 days post peak.

6. Light-curve Modeling

SN 2020wnt was no ordinary SN. Nonrotating, neutrino-powered, CCSNe generate inadequate energy and ^{56}Ni to explain its evolution (Ertl et al. 2020). If collisionally powered at peak, a large amount of matter would be required at distances $\sim 10^{15}$ cm. The radio limits on mass loss after the peak would require discontinuous mass ejection. Similarly, the dip in the light curve at $\sim$20 days would be difficult to explain without

Table 1
Models for SN 2020wnt

Model	J_0 (10^{53} erg s)	$M_{\rm preSN}$ ($M_\odot$)	$M_{\rm Fe}$ ($M_\odot$)	$M_{\rm cut}$ ($M_\odot$)	$E_{\rm ej}$ (10^{51} erg)	$M_{\rm ej}$ ($M_\odot$)	$M_{\rm Ni}$ ($M_\odot$)	$J_{\rm Fe}$ (10^{49} erg s)	$E_{\rm puls}$ (10^{51} erg)	$B_{\rm puls}$ (10^{14} G)	$f_{\rm ej,puls}$	Comments
C95	0	95.0	0.0	0.0	37.2	95.0	2.85	0.0	0.0	⋯	⋯	CO core; no $\dot{M}$; PISN
C100	0	100.0	0.0	0.0	43.7	100.0	5.13	0.0	0.0	⋯	⋯	CO core; no $\dot{M}$; PISN
C105	0	105.0	0.0	0.0	48.6	105.0	10.6	0.0	0.0	⋯	⋯	CO core; no $\dot{M}$; PISN
He20	0	16.95	1.94	2.00	5.0	14.94	0.88	0.0	1.2	2.0	0.54	He core; no rot.; CSM
T50	1.5	28.36	2.41	2.50	15.0	25.86	0.85	2.4	2.0	2.0	0.41	ZAMS; Rapid rot.; CSM
T70	3.5	41.84	2.70	2.50	19.1	39.34	1.71	3.9	2.0	2.0	0.34	ZAMS; Rapid rot.; PPISN

Notes. The initial mass is the numerical part of the model name, and J_0 is its total angular momentum. Models with $J_0 = 0$ are not rotating. $M_{\rm Fe}$ is the mass of the pre-SN iron core, and $M_{\rm cut}$ the location of the piston used to eject all exterior mass. Explosion energy includes work done by the piston and magnetar minus pre-SN binding energy and energy emitted as light. $M_{\rm ej}$ is the total mass ejected and equals $M_{\rm preSN}$ - $M_{\rm cut}$. $J_{\rm Fe}$ is the final angular momentum inside the mass cut. $M_{\rm Ni}$ is the ejected mass of ^{56}Ni. $E_{\rm puls}$ is the initial rotational energy of the embedded magnetar with the magnetic field of $B_{\rm puls} = 2 \times 10^{14}$ G, when one is present. $f_{\rm ej,puls}$ is the mass fraction of the ejecta directly heated by the magnetar. "ZAMS" in the Comments column indicates that the star began its life as a hydrogen-rich star on the main sequence. Other initial models were helium or carbon-oxygen cores. Models with a "CSM" were surrounded by a pre-SN stellar wind.

some sort of explosive shell event months to years before the star died. Instead, the broad smooth light curve at peak is more suggestive of diffusion than shock interaction.

Other options require either a thermonuclear explosion, i.e., a pair- (PISN) or pulsational pair-instability supernova (PPISN), or rapid rotation and a central engine. Unmodified PPISNe are too low in energy to explain SN 2020wnt (Woosley 2017); PISNe require the retention of a large amount of mass; and rapid rotation is damped by mass loss. This means that successful models will be favored by low mass loss, and presumably low metallicity (e.g., Woosley & Heger 2006), or require special circumstances, like a binary merger (e.g., de Mink et al. 2013; Marchant et al. 2019).

If attributed to diffusion, the broad main peak requires a large mass of hydrogen-poor ejecta, well in excess of 10 $M_\odot$, with characteristic speeds in excess of 6000 km s^{-1} (from nebular spectra). Taken together, this implies an explosion energy in excess of $\sim 5 \times 10^{51}$ erg. Besides the fact that no neutrino-powered model has ever achieved such a high terminal energy, nonrotating stars with helium core masses this large are expected to collapse entirely to black holes (Ertl et al. 2020). We thus expect, from basic principles, that any successful model for SN 2020wnt is going to involve rotation and be relatively "nonstandard." The initial 5–10 day spike also requires its own explanation. True shock breakout from a compact stripped star generates a faint, very brief transient in the soft X-ray band (Tolstov et al. 2013), quite unlike what was observed here.

Here, we present models (Table 1) computed using the KEPLER code (Weaver et al. 1978; Woosley et al. 2002; Woosley 2017). For three PISN models, C95, C100, and C105, carbon-oxygen cores were evolved without mass loss through their stable carbon and neon-burning phases and explosion. Due to the nearly fully convective nature of very massive stars during helium burning, even mild mass loss will uncover the CO core in a star that has lost its hydrogen envelope, so pure CO stars are a reasonable starting point. For a lighter model, He20, a 20 $M_\odot$ helium star was evolved until iron core collapse including mass loss according to Yoon (2017). Two others, T50 and T70, assumed rapid rotation that led to chemically homogeneous evolution on the hydrogen-burning main sequence. These stars were evolved until iron core collapse including mass loss, according to Nieuwenhuijzen & de Jager (1990) and Yoon (2017). Except for the PISN, all pre-SN models were exploded using a piston situated near the edge of their iron cores and moved so as to generate a desired terminal kinetic energy. SN light-curve calculations assumed an opacity due to electron scattering plus a background opacity due to lines of 0.03 cm^2 g^{-1}. This is applied to all models except for the T70 PPISN model, for which we use a background opacity of 0.01 cm^2 g^{-1}, which provides a significantly better fit to the data. We recognize the extreme uncertainty in the mass-loss rate in very massive stars, and emphasize that the relevant stellar parameters are those at the time of core collapse.

Figure 9 compares the bolometric light curves of these models to the observed bolometric light curve.

6.1. A Poor Match with Pair-instability Supernovae

Figure 9 (left) shows the bolometric light curve of SN 2020wnt in comparison with PISN models, both from the literature and newly computed. We plot a bolometric light curve of the 100 $M_\odot$ hydrogen-poor PISN model from Kasen et al. (2011), along with the three new models of PISN progenitor stars based on 95, 100, and 105 $M_\odot$ carbon (10%) and oxygen (90%) cores. These are models C95, C100, and C105 from Table 1. The velocity and composition profiles of the C100 model are shown in Figure A2 (left). In PISNe, the explosion energy, ^{56}Ni mass, and total mass are all inextricably entwined and cannot be varied independently. If the peak is powered entirely by radioactivity, then we determined the ^{56}Ni mass to be about 5–10 $M_\odot$. For a PISN, this requires a core mass close to 100 $M_\odot$, much more than what we derived from the rise time of SN 2020wnt. The three PISN models illustrate this issue more concretely: models that are bright enough (C105) peak too late and models that peak early enough (C100) are too faint. Though the ^{56}Ni mass and expansion speed of Model C100 is in reasonable accord with observations, its long rise time and broad peak are not. Further, the explosion time of SN 2020wnt is well determined, so one cannot arbitrarily shift the time of peak to better fit the data. The introduction of metallicity (Kozyreva et al. 2017), mixing (Kozyreva & Blinnikov 2015; Gilmer et al. 2017), multidimensional calculation (Chen et al. 2014), and rotation (Chatzopoulos et al. 2013, 2015) affect the rise time and peak luminosity of PISNe, but not enough to match our observations of SN 2020wnt. Thus, we disfavor a classical PISN as the explosion mechanism for SN 2020wnt.

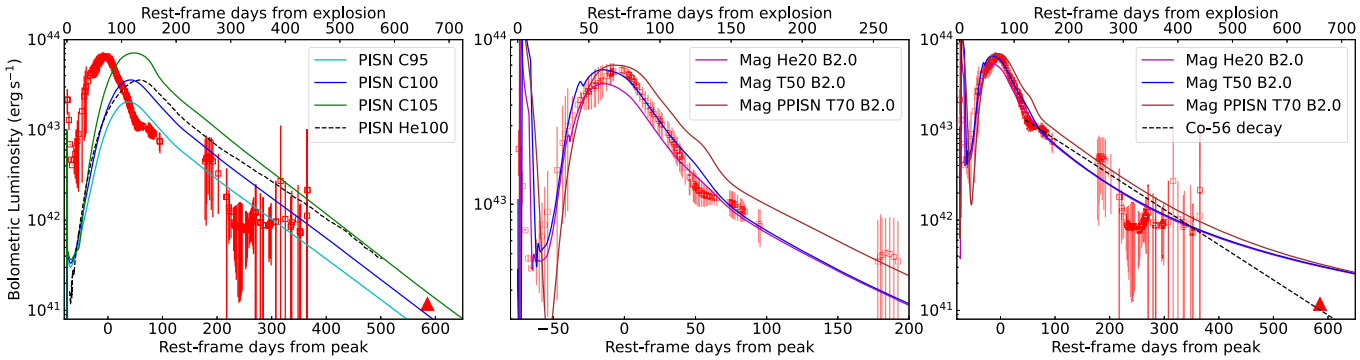

Figure 9. Bolometric light curve of SN 2020wnt compared with PISN (left) and magnetar models (center and right) discussed in Section 6. The red triangle denotes the lower limit of the bolometric luminosity obtained from the HST observations of SN 2020wnt 585 days post peak. PISN models with the 100 $M_\odot$ He star from Kasen et al. (2011) along with three new hydrogen/helium-poor models with 95, 100, and 105 $M_\odot$ are plotted with dotted lines. The comparison shows that PISN models rise too slowly to explain SN 2020wnt's peak luminosity. For the magnetar models, the center and right panels display different timescales. Models He20, T50, and T70 are shown; they are explosions of a massive progenitor star with energy boost from a central engine. A magnetar is invoked in the three models, but an accreting black hole would serve the same purpose. The magnetic field of the magnetar is 2×10^{14} G for all models. Even though the light curves are powered at peak chiefly by the magnetar, ^{56}Co decay contributes about a quarter to a half of the luminosity on the tail, hence the difference between Model T70 and Models T50 and He20; see detailed discussions of these models in Section 6. The left and right panels show the light curve around peak and the entire light curve, respectively. These models provide markedly better fits to the data compared to the PISN models. The PISN and magnetar model data are available as the data behind the figure.

(The data used to create this figure are available.)

6.2. Models That Include a Magnetar and Radioactivity

With the only explosion mechanism known to produce a sufficient amount of ^{56}Ni to power the peak of SN 2020wnt ruled out, we consider an additional power source from a central engine. Though black hole accretion might be involved, the central engine is more easily parametrized as a magnetar. A constraint from the spectroscopic observations is that the central engine must be embedded and invisible during the optically thick phase to explain the lack of its spectroscopic signatures. Thus, the central engine's energy output must be significantly smaller than the explosion energy, resulting in only the innermost ejecta directly affected by its heating. An energetic explosion is still required to give the requisite combination of high velocity and a long diffusion time. A successful model will thus almost certainly make appreciable ^{56}Ni as well. In general, the models we consider have the rise time set by the ejecta mass and the explosion energy; the peak luminosity is set by the magnetar rotational energy; and the late-time luminosity set by the magnetic field of the magnetar. Figure 9 (center and right) shows light curves from magnetar models in Table 1. Figure A3 shows light curves from the same models, but with contributions from radioactivity, the magnetar, and CSM interactions explicitly shown.

These models resemble those of Dessart (2019), but differ in focusing on more massive explosions with longer rise times. Some of our models also include rotation and interaction with a CSM. However, the radiation transport and spectra are better treated in Dessart (2019).

6.2.1. Lower-mass Nonrotating Helium Star with Magnetar and Circumstellar Medium Interaction

Model He20 (Table 1) is a nonrotating 20 $M_\odot$ helium star with initial metallicity 10% solar that evolves including mass loss according to Yoon (2017). It resembles Model r0e2 of Dessart (2019), but has a larger ejected mass, 14.9 $M_\odot$ versus 9.7 $M_\odot$, and therefore a longer rise time. An artificial explosion was induced using a piston located at 2.00 $M_\odot$, which was moved sufficiently rapidly to eject all external matter with high speed. The asymptotic kinetic energy of the ejecta was 4.3×10^{51} erg. Because of the deeply situated piston and shallow density gradient outside, substantial ^{56}Ni was synthesized, 0.88 $M_\odot$. This large kinetic energy and nickel mass are inconsistent with a neutrino-powered explosion (Ertl et al. 2020), so formation of a rapidly rotating pulsar or accretion onto a black hole is implicitly assumed, even though rotation was neglected in the evolution. The model resembles those that have been proposed for gamma-ray bursts (e.g., MacFadyen & Woosley 1999; Woosley & Bloom 2006), but does not involve the escape of a relativistic jet.

The light curve of the unmodified, radioactive model peaks below 10^{43} erg s^{-1}, far too faint to explain SN 2020wnt. Indeed, producing the peak of the light curve using radioactivity alone would require almost an order of magnitude more ^{56}Ni, about 7 $M_\odot$. This would require a large explosion energy, which would greatly reduce the diffusion time and exclude models of such low mass. It would also require more ^{56}Ni than is physically credible for the density gradient surrounding the iron core in Model He20. Raising the explosion energy in this model to the extreme 3.5×10^{52} only increases the ^{56}Ni production to 1.22 $M_\odot$. Such a large energy would require a massive neutron star (Metzger et al. 2015). The pulsar would also not develop its full energy for a few seconds after collapse while the proto-neutron star cooled by neutrino emission. During that time, additional material would accrete on the proto-neutron star.

The effect of adding a magnetar was thus explored. An initial rotation rate of 4 ms, corresponding to a rotational energy of 1.2×10^{51} erg, was assumed, and a constant magnetic field of 2.0×10^{14} G. The energy deposition formula of Woosley (2010) was used, which differs slightly from Kasen & Bildsten (2010). Energy was uniformly deposited in the inner 100 zones of ejecta (0.54 $M_\odot$). This energy both illuminates the SN and inflates a low-density bubble bounded by a high-density shell out of which the trapped energy diffuses. It is important that the magnetar energy, 1.2×10^{51} erg, is considerably less than the background SN kinetic energy, 4.3×10^{51} erg. Consequently, in our one-dimensional study, the bubble of pulsar heated

energy does not erupt outside of the photosphere before the light-curve peaks. It remains bounded within the inner 7.62 $M_\odot$ of the 14.9 $M_\odot$(51%) ejecta and ultimately all moves at a nearly constant speed of 4400 km s^{-1}. In reality, multi-dimensional effects would lead to the broadening of the high-density bounding the bubble by an order 10%–29% in radius (Chen et al. 2016) and the swept-up matter would not all move at constant velocity. This level of thickening would not lead to fingers of plasma extending above the photosphere until well after peak, and this might have consequences for the spectroscopic history (Kasen et al. 2016; Dessart 2019). The model light curve peaked at 65 days with a luminosity 4.7×10^{43} erg s^{-1}. The photosphere reached the edge of the magnetar-inflated bubble about 80 days later, but this is a very approximate number given multidimensional effects and the simplifying assumptions made in KEPLER for radiation transport (e.g., spherical symmetry, single temperature, and simple opacity assumptions).

As Figure 9 (right) shows, radioactivity plus an embedded magnetar replicates the broad features of the bolometric light curve near peak and on the tail, with the bulk of the energy being provided by the magnetar. Full trapping of magnetar-deposited energy is assumed, even though that is probably unlikely at the latest times plotted. The light curve shown is thus an upper bound for the magnetar contribution. On the other hand, even a slight decrease in the magnetic field would give a light curve that was brighter at late times.

The magnetar plus radioactivity model alone still fails to account for the bright transient lasting about a week at the beginning of the SN. That feature is almost certainly due to CSM interaction. The outer 0.02 $M_\odot$ of Model He20 has a speed in excess of 20,000 km s^{-1} and carries 1.1×10^{50} erg, more than enough to explain the initial display, provided that ejecta interacted with a comparable mass inside $\sim 10^{16}$ cm. Figure 9 (center and right) includes the effect of adding pre-explosive mass loss around the SN. A high mass-loss rate is necessary to explain the initial bright peak, but the same mass loss would overilluminate the dip at ~20 days. One must therefore make the reasonable assumption that the mass loss increased as the star neared its death. We have in mind the acoustic transport of convective energy during the post-carbon-burning stages as discussed by Shiode & Quataert (2014), Fuller & Ro (2018), and Leung et al. (2021). Here, a mass-loss rate of 0.0015 $M_\odot$ yr^{-1} was adopted during years 3.75–0.75 before iron core collapse, rising to 0.01 $M_\odot$ yr^{-1} in the final 0.75 yr, for a total CSM mass of 0.012 $M_\odot$. This CSM mass is roughly consistent with what is predicted by Leung et al. (2021). A steady wind speed of 500 km s^{-1} is assumed, but other values of mass loss and wind speed would also give similar results, provided that $\dot{M}/v_{\rm wind} \sim 10^{15}$–$10^{16}$ g cm^{-1} during the last few years. A still smaller mass-loss rate at earlier times might characterize the tail of the light curve.

6.2.2. A More Massive Magnetar Model with Rotation

Now consider a more massive model evolved from the main sequence including mass loss and rapid rotation. Similar models have been considered for the progenitors of gamma-ray bursts and SLSNe Ic (Woosley & Bloom 2006; Aguilera-Dena et al. 2018). Model T50 begins its life as a 50 $M_\odot$ main-sequence star with 10% solar metallicity and an equatorial rotational speed of 240 km s^{-1}. The velocity and composition profiles of the T50 model are shown in Figure A2 (right). The initial angular momentum of the star on the zero-age main sequence was 1.5×10^{53} erg s. With this large rotation rate, this star evolved chemically homogeneously, burning most of its hydrogen on the main sequence and avoiding red giant formation. It thus avoids the large shedding of mass and angular momentum that would occur in that phase. Using the Yoon (2017) mass-loss rate appropriate for 10% solar metallicity after central hydrogen depletion, the pre-SN star had a mass of 28.36 $M_\odot$ and an iron core of 2.41 $M_\odot$. There was a sharp falloff in density at the base of the oxygen shell at 2.50 $M_\odot$. The matter interior to 2.50 $M_\odot$ had an angular momentum of 2.4×10^{49} erg s. If it collapsed to a neutron star, that compact remnant would have a gravitational mass of about 2.1 $M_\odot$ and a submillisecond rotation period.

While the subsequent evolution of such a core is uncertain, it is plausible that some fraction of the available several $\times 10^{52}$ erg rotational energy of a massive, submillisecond pulsar (Metzger et al. 2015) will be released in about a second. Accordingly, a piston was situated at 2.50 $M_\odot$ and moved so as to produce an asymptotic kinetic energy 1.37×10^{52} erg. The actual work done by the piston was larger, 1.67×10^{52} erg, since the net binding energy of the pre-SN star external to 2.50 $M_\odot$ was 3.05×10^{51} erg. The explosion also produced 0.85 $M_\odot$ of ^{56}Ni. If the piston had been situated deeper, this ^{56}Ni mass might be increased by at most a few tenths of a solar mass, but not much more.

Even with a higher ^{56}Ni mass, the resulting light curve would still fail to match that of SN 2020wnt. To agree with observations, the light curve must again be supplemented with a central energy source to boost the peak luminosity, and CSM interaction to explain the initial peak. In order to boost the speed of the inner ejecta and provide a slightly greater luminosity at peak, a magnetar of slightly greater initial rotational energy, 2×10^{51} erg ($P = 3$ ms), was used here instead of the slower rotating 1.2×10^{51} erg used for Model He20. The magnetic field, 2.0×10^{14} G, which sets the late-time luminosity, was the same. Because of its greater energy, the model was also surrounded by a slightly more massive CSM, 0.015 $M_\odot$, again consisting of two shells, 0.001 $M_\odot$ yr^{-1} for years 6 to 1 before explosion and 0.01 $M_\odot$ yr^{-1} for the last year. The resulting light curve is shown in Figure 9 (center and right). The final kinetic energy of the ejecta in the magnetar model is 1.50×10^{52} erg, which includes 1.37×10^{52} erg of net energy from the piston, 2×10^{51} erg for the magnetar, less 0.7×10^{51} erg radiated as light. Due to the action of the magnetar, the inner 10.6 $M_\odot$ of the 25.8 $M_\odot$ of ejecta (41%) was accelerated into a thin shell moving at 5700 km s^{-1}. The model had a peak luminosity of 6.6×10^{43} erg s^{-1} 60 days after the explosion. The magnetar-inflated bubble was still well below the photosphere at that time, and would not reach the photosphere until approximately 150 days post peak. As mentioned earlier, this number is very approximate due to the simplifying assumptions made by KEPLER.

6.2.3. Pulsational Pair-instability Model plus Central Engine

Pulling out all the stops, we considered the most massive credible model for SN 2020wnt, a PPISN plus magnetar. A more massive model would either eject so much mass during its pulsations that a very different light curve would result (Woosley 2017), or explode completely as a PISN. For the assumed reaction rates, and hence central carbon mass fraction at helium exhaustion, the PI is first encountered for pre-SN core

masses $\gtrsim$35 $M_\odot$. Though often thought of as a violent instability ejecting solar masses of material at a time, on its lighter end, in the less massive, presumably more abundant stars, the PI only causes a series of weak pulses that cumulatively eject a few solar masses or less at moderate speeds (few 1000 km s^{-1}) over a period of a several days. The remaining star then collapses to a black hole or neutron star (see, e.g., the 38 $M_\odot$ model in Table 1 of Woosley 2017). If all the remaining star did was collapse to a black hole, this sort of model would only produce a very faint, brief transient coming from the small internal energy of the ejected helium and heavy elements. If, however, iron core collapse somehow leads to an energetic explosion, the interaction with several solar masses of ejecta has interesting implications for the early light curve.

Model T70 (Table 1) began its life as a 70 $M_\odot$, rapidly rotating main-sequence star with 10% solar metallicity similar to Model T50, but with greater mass and angular momentum, 3.5×10^{53} erg s. The equatorial rotation speed was 380 km s^{-1}, or about 20% the Keplerian speed. The star again experienced CHE and mass loss, ending its life as a rapidly rotating core of mostly carbon, oxygen, and heavier elements. For the pre-SN star, the mass interior to the mass cut at 2.50 $M_\odot$ had angular momentum 3.9×10^{49} erg s, sufficient to make a submillisecond pulsar with gravitational mass roughly 2.1 $M_\odot$ if black hole formation was avoided. Indeed, the inferred rotation rate would be about 0.4 ms, suggesting rotation would play a large role in the iron core's subsequent contraction and evolution.

Before dying, the star became unstable to nuclear energized PI pulsations in the oxygen-burning shell after a silicon-burning core had already been established. Dozens of weak pulses ejected a total of 3.2 $M_\odot$ with a typical speed of 2000–4000 km s^{-1} and a total energy of 2.3×10^{50} erg. By the time the core collapsed this matter had coasted to radii $\sim 10^{13}$–10^{14} cm, forming something that resembled a red supergiant envelope around the collapsing core.

An explosion was simulated with a piston at 2.50 $M_\odot$ with a terminal kinetic energy of 1.76×10^{52} erg, plus binding energy, 4.8×10^{51} erg, for a total of 2.24×10^{52} erg. Because of the deep mass cut, even slightly into the iron core itself, the shallow density gradient outside this core, and a very energetic explosion, the model ejected 1.8 $M_\odot$ of ^{56}Ni, which we regard as close to an upper bound. Raising the explosion energy to 3.5×10^{52} erg only increased the ^{56}Ni mass to 2.25 $M_\odot$. The blast also interacted with the 3.2 $M_\odot$ of slow moving ejecta from the prior pulsations producing the "breakout" transient. The sharp dip at about 20 days would have been brighter if the pulsations had ejected their matter just a bit sooner or if there were a wind of only 0.001 $M_\odot$ yr^{-1} prior to the pulsations.

Like previous models, even this extremely massive model cannot produce SN 2020wnt's light curve without a central engine. The model light curve in Figure 9 (center and right) shows the effect of adding a magnetar with initial rotational energy 2×10^{51} erg and magnetic field 2.0×10^{14} G. The light curve peaks at 63 days with a luminosity of 8.1×10^{43} erg s^{-1}. The magnetar accelerates the inner 13.5 $M_\odot$ of the 39.3 $M_\odot$ ejecta (34%) to a constant speed of 5100 km s^{-1}. Similar to other magnetar models, the effects of the magnetar are well hidden at peak.

6.3. Best-fit Model for SN 2020wnt

Three promising models for SN 2020wnt involving similar central engines have been considered. Magnetars are responsible for producing the peak of the light curve in all of them, and CSM interaction produces the bright initial transient. For the two models with winds, He20 and T50, the rapid decline and sustained emission at around 20 days implies a mass-loss rate that increased just before the star died. The required loss rates, 0.01–0.001 $M_\odot$ yr^{-1} during the last several years, are consistent with predictions by Shiode & Quataert (2014) and Leung et al. (2021).

The maximum ^{56}Ni mass seen in any calculation, even the most massive possible model with the deepest mass cut and an explosion energy near 4×10^{52} erg, was 2.25 $M_\odot$. This is inadequate to explain the light-curve peak, though such a large amount of ^{56}Ni would still have consequences for the spectrum and for the light curve on the tail. Due to the large ^{56}Ni mass required for radioactivity alone to power the light curve, along with our spectrum at a later epoch showing magnetar signatures, we disagree with Gutiérrez et al. (2022) and favor a magnetar model.

None of the simple magnetar-powered models reproduced the dip seen on the tail of the light curve, which is likely due to dust formation. We also note the discrepancy between the model and the data around 150 days post peak in the nebular phase. A possible culprit is that the observations at those epochs only contain two bands, r and i, both of which have strong emission lines, likely leading to overestimation of the (uncertain) bolometric luminosity. However, we note that Gutiérrez et al. (2022) found a similar bolometric light-curve shape at this epoch using photometry from more bands. Another possibility for this discrepancy is additional power from weak CSM interactions unaccounted for by our models.

KEPLER does not compute spectra, yet from the small interaction radius, $\sim 10^{14}$ cm, and high luminosity, $\gtrsim 10^{43}$ erg s^{-1}, of the breakout transient, we can confidently say that the model spectrum at that stage would have been very blue. Indeed, much of the light during the breakout transient may have been emitted in the far-ultraviolet, and we only observed the tail of the blackbody radiation. The observed $g - r$ color was indeed blue (Figure 2), indicating a large bolometric correction. Closer to the main peak, typical effective temperatures were $\sim$8000 K. The photosphere at peak was still in the outer part of the ejecta, outside of the magnetar-inflated bubble, due to the relatively low magnetar energy compared to the kinetic energy and the high ejecta mass. In that case, it may be difficult to distinguish, even spectroscopically, between an embedded magnetar and radioactivity as the primary power source.

While we have emphasized a magnetar energy source for the peak luminosity, black hole accretion from fallback is an interesting alternative if a neutron star did not form (MacFadyen et al. 2001; Dexter & Kasen 2013; Moriya et al. 2019). This might be expected in such massive progenitor stars. The time history of this accretion is difficult to predict, however, given the uncertain angular momentum distribution in the ejecta and the role of the reverse shock (Dexter & Kasen 2013).

7. Comparison to Model Spectra

7.1. Nebular Spectrum Comparison

In the nebular phase, the ejecta are optically thin, which allows our observations to measure their composition and constrain their properties, including the total mass. We

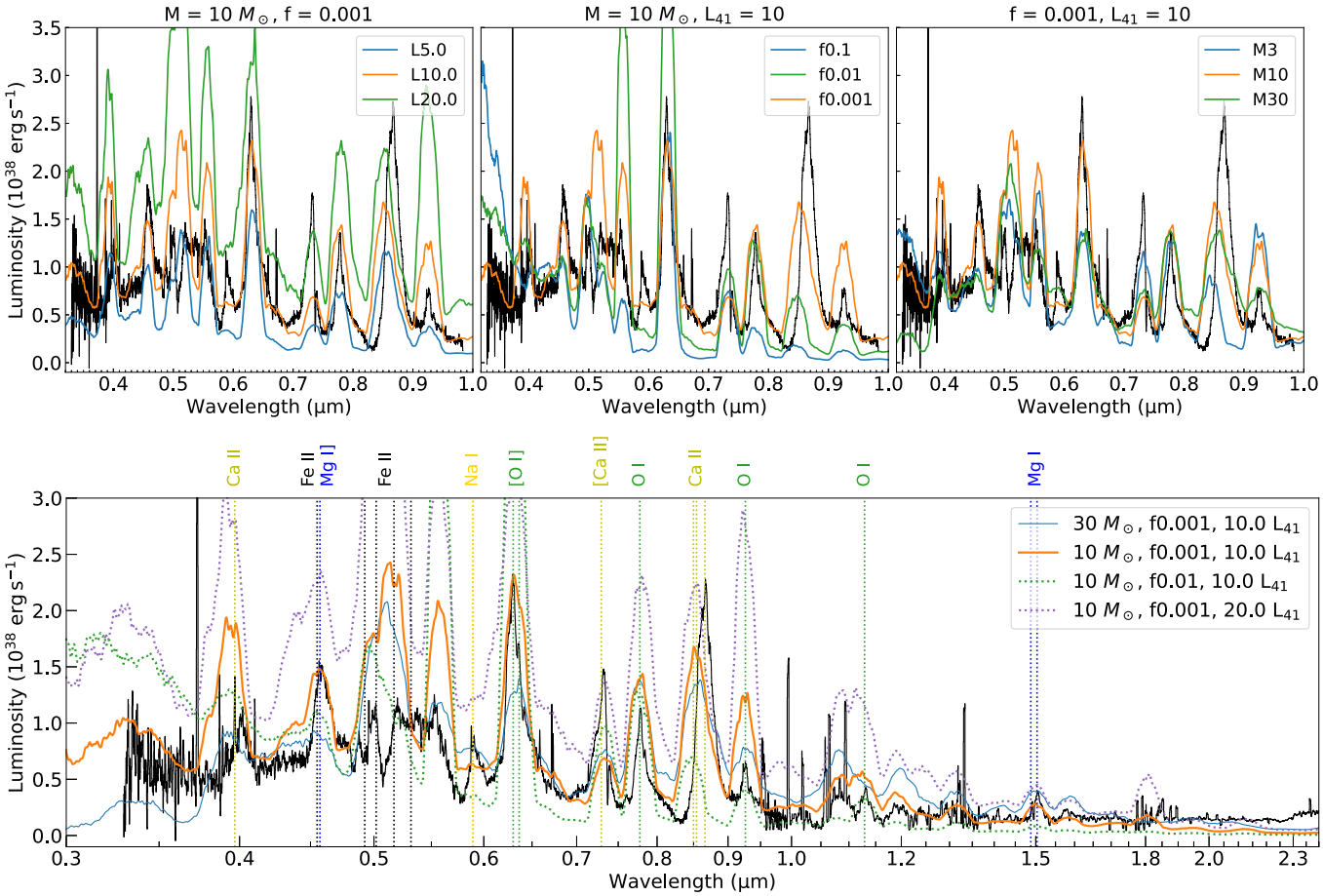

Figure 10. Comparisons between a nebular-phase spectrum of SN 2020wnt and models from Jerkstrand et al. (2017). Top row compares the optical part of the spectrum with models with varying parameters. The model names, e.g., M10 f0.001 L10, refers to the model with 10 $M_\odot$ of ejecta mass, a filling factor of 0.001, and an energy deposition rate of 10^{42} erg s^{-1}. Similarly, L_{41} refers to the unit of 10^{41} erg s^{-1}. Panels from left to right show models with varying energy deposition rate, filling factor, and mass, respectively. The best-fit model, M10 f0.001 L10, is plotted with the same color in all panels. Bottom shows a similar comparison, but with the entire optical–NIR spectrum. Note that the x-axis is in a logarithmic scale. Four models are shown here for comparison. The same best-fit model, M10 f0.001 L10, is again plotted in the same color as in the top panels.

compare our optical to near-IR spectra from 301 to 313 days post peak (about 378 days post explosion) to the single-zone model grid from Jerkstrand et al. (2017), computed using the SUMO code. To prepare our data for this comparison, we perform absolute flux calibration of the optical spectrum by matching it to the flux observed in the r band at that epoch. We then scale the near-IR spectrum to match the optical in the overlapping region. The models are computed at 400 days post explosion assuming ejecta velocity of 8000 km s^{-1} to set the physical volume of the ejecta containing the mass $M_{\rm ej}$. While these numbers are not exactly the same as the epoch of observation and ejecta velocity of SN 2020wnt, the grid is too coarse for these small differences to matter. The models assume 100 spherical clumps of ejecta within this volume, taking up a filling factor of f. This factor sets the density within each clump: smaller f results in a larger density. The models account for only the oxygen-rich zone of the ejecta, which is responsible for most of the emission lines observed at these epochs. By not including other subdominant zones, these models are less computationally intensive and are ideal for parameter space exploration. We only consider full-carbon-burning composition models from the paper (and not the pure-oxygen or the oxygen-magnesium models). The ejecta composition in these models is 74% O, 15% Ne, and 7% Mg. The model grids we use are computed over ejecta masses of 3, 10, and 30 $M_\odot$ (only oxygen-rich zone); filling factors of 0.1, 0.01, and 0.001; and powering luminosities of 2.5, 5, 10, and 20×10^{41} erg s^{-1}. The model is agnostic to the nature of the source of the powering luminosity, though the paper provides discussions on how clumpy ejecta could be indicative of a central engine. From our bolometric light curve, the luminosity at the epoch of the spectra is about 10^{42} erg s^{-1}.

Figure 10 shows select results from this comparison. The top three panels compare the optical part of the spectrum to models with varying powering luminosity, filling factor, and mass, respectively. The relationship between the luminosity and the resulting spectra is straightforward: larger powering luminosity results in larger observed luminosity, with modest effect on the line shapes and ratios. Shown in the top-left panel, we find that models with $L = 10^{42}$ erg s^{-1}, similar to the bolometric luminosity at this epoch, provide the best fit visually to the data.

The next parameter we consider is the filling factor, which sets the density of the ejecta clumps (top-middle panel). Consequently, this parameter strongly affects the temperature and the line ratio. The $f = 0.1$ model is the least dense and thus gets very hot, overpredicting the flux in the blue while underpredicting the red continuum and the line fluxes. The

$f = 0.01$ model does better at matching the O I 7774 Å line, but is still overpredicting the blue flux and other line fluxes, primarily the [O I] 6300, 6363 Å lines. Lastly, the clumpiest $f = 0.001$ provides the best fit to the data by simultaneously fitting the continuum across the optical band and providing a decent fit to both the [O I] 6300, 6363 Å and O I 7774 Å lines. It is also the only model that fits the Mg I] 4571 Å line.

Lastly, we consider different ejecta masses in the right panel. The differences between the three masses considered in this model grid are relatively subtle, with the [O I] 6300, 6363 Å lines being the most sensitive mass indicator. Our observation is best explained here by the moderate 10 $M_\odot$ model, with the other two masses producing poorer fits to the O lines, including in the near-IR. Further, it is the only model that can satisfactorily fit the Mg I] 4571 Å and Mg I 1.5 μm lines.

We note, however, that some line predictions are still off in our best-fit model. For instance, the [Ca II] 7292 Å and the Ca triplet are poorly fit. The region between 5000 and 6000 Å, which has many Fe lines, is also poorly fit. These discrepancies are most likely because features from these species do not come from the oxygen-rich zone considered in these models. The ratio between the O I 7774 Å and 9263 Å lines is different from the observed ratio, and the modeled line width is also larger than what is observed. As discussed by Nicholl et al. (2019), this could be evidence that the central engine is ionizing the innermost ejecta (smallest velocity), producing these narrow O recombination lines. The presence of a central engine would also be consistent with the highly clumpy ejecta (small filling factor) that we infer. Further investigation using multizone ejecta models will produce a more realistic map the massive ejecta of SN 2020wnt.

We finally note that Dessart (2019) performed a spectroscopic modeling work using `CMFGEN` for a grid of magnetar-powered SLSNe. However, the range of explosion and magnetar parameters explored does not cover the parameters appropriate for SN 2020wnt. The models presented in that paper only have a maximum rise time of 52 days, much too short for SN 2020wnt. Models with rise times longer than 40 days (r0e1, r0e2, and r0e2ba) have very small velocity and/or small luminosity, incompatible with SN 2020wnt.

As a cursory comparison, we plot the model r0e2cl alongside our data and the best-fit model from Jerkstrand et al. (2017) in Figure A4. The r0e2cl model incorporates clumpy ejecta and is found by Dessart (2019) to best reproduce the nebular spectrum of SN 2007bi. We scale the Dessart (2019) model to match the [O I] 6300, 6363 Å flux. The continuum prediction from both models differ significantly. The Dessart (2019) model notably better fits the Fe II features around 5000 Å and the profile of the [Ca II] doublet at 7300 Å. Otherwise, the Jerkstrand et al. (2017) model fits the data better, including in the continuum. Future work is necessary to extend the parameter space explored using the method of Dessart (2019) to realistically fit the data of SN 2020wnt or other SNe like it.

7.2. Spectroscopic Comparison with Massive Core-collapse and Pair-instability Models

Figure 11 shows a comparison between the HST/WFC3 spectrum of SN 2020wnt at 378 days post peak and the models of massive CCSNe and PISNe from Mazzali et al. (2019). The observed spectrum, plotted in gray, shows a clear continuum still at this epoch. Some contribution to this continuum comes from the underlying H II regions in the host galaxy. However, we note that there is P Cygni absorption associated with the 1.08 μm line, which demonstrates that some of the continuum is intrinsic to the SN.

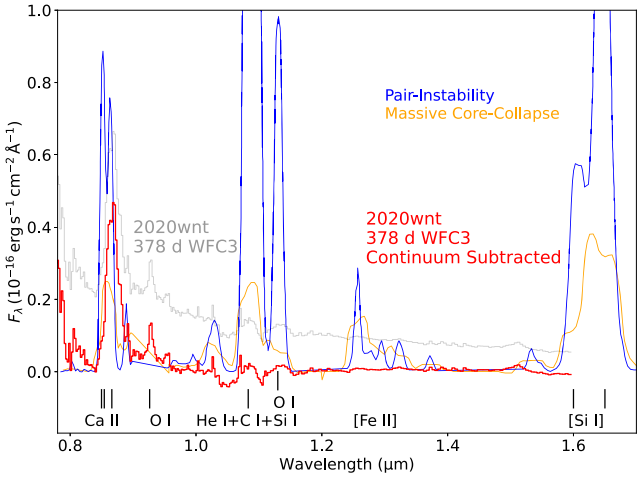

Figure 11. Comparison between the near-IR spectrum of SN 2020wnt obtained at 378 days post peak with HST/WFC3 near-IR grisms and models of nebular spectra from a massive CCSN (orange) and a PISN (blue) from Mazzali et al. (2019). The models have been scaled to the distance of SN 2020wnt. The gray line shows the observed spectrum, which clearly has some continuum. While the underlying host may contribute, the P Cygni absorption associated with the 1.08 μm feature shows that some of the continuum is intrinsic to the SN. We estimate and subtract the continuum by fitting a low-order polynomial. The continuum-subtracted spectrum is shown in red.

The model spectra from Mazzali et al. (2019) were computed to fit the observations of SN 2007bi at about 367 days post peak. Here, we scaled the models to the distance of SN 2020wnt (141.8 Mpc from SN 2007bi's 592 Mpc used in the paper). The massive CCSN model assumes 33 $M_\odot$ of ejecta mass with an explosion energy of 3×10^{52} erg. The explosion produces 4.5 $M_\odot$ of ^{56}Ni. These parameters are in agreement with what we derived for SN 2020wnt, if we assume that the SN is powered by radioactivity (note the caveats from Section 6). A core-collapse explosion with such an energy does not come from a normal neutrino-driven explosion. The PISN model shown here is from the 100 $M_\odot$ model with an ejecta mass of 94 $M_\odot$ and a ^{56}Ni mass of 3.1 $M_\odot$. The main distinguishing features in the near-IR between these two classes of models are the strengths of the [Si I] lines around 1.60 and 1.65 μm and the line complex at 1.08 μm.

In comparison to the models, SN 2020wnt at 378 days post peak does not show any of the strong forbidden lines predicted by the PISN model. Specifically, the PISN model predicts strong lines around 1.08 μm from [S I] and the [Fe II] complex around 1.25 μm, in contrast with the observations. In general, the line strengths observed in SN 2020wnt are much closer to those predicted by the massive core-collapse model. One major exception is that the [Fe II] complex around 1.25 μm, also predicted by the core-collapse model, is still missing. This could be because the spectrum of SN 2020wnt does not appear to be completely nebular yet, and a later NIR spectrum would be crucial to make a more robust model comparison. However, the lack of distinct PISN features is another argument against SN 2020wnt originating from a PI explosion.

8. Host Properties

WISEA J034638.04+431348.3 is the host galaxy of SN 2020wnt. It is a faint dwarf galaxy, with irregular

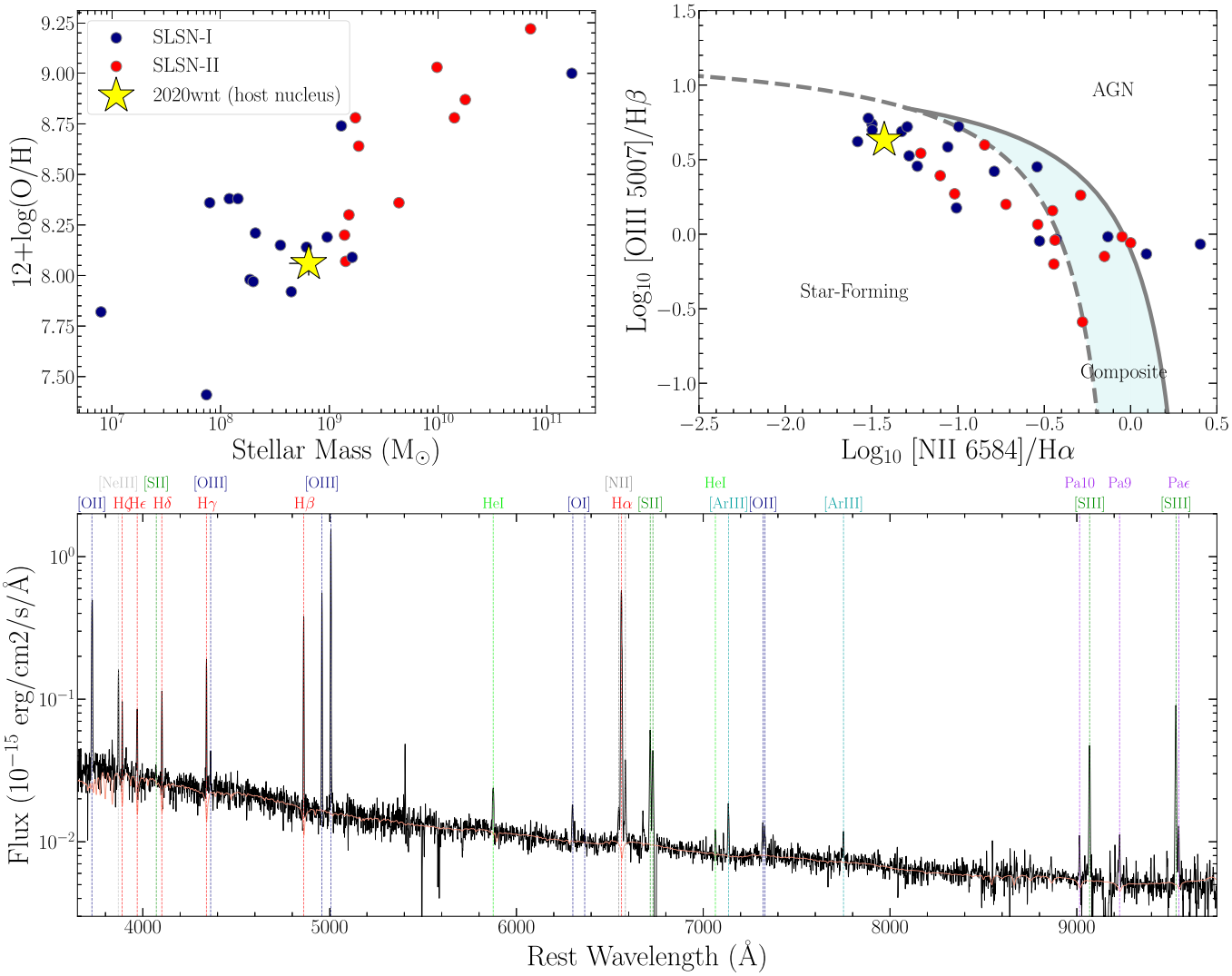

Figure 12. Top left: stellar mass vs. host-galaxy metallicity of SN 2020wnt (yellow star) vs. SLSNe I (blue circles) and SLSNe II (red circles) from Perley et al. (2016). Top right: BPT diagram showing 2020wnt is consistent with the star-forming galaxy population. Bottom: a Keck/LRIS spectrum of the host-galaxy nucleus of SN 2020wnt. Overplotted in tangerine is the best-fit SED model for the galaxy stellar continuum that is subtracted before measuring line fluxes. Strong emission lines are identified. Notably, the auroral oxygen lines of [O III] λ4363 and [O II] λ7320,7330 are present, allowing a direct metallicity measurement.

morphology and no prior spectroscopic redshift. To measure the host-galaxy redshift, we use the Keck/LRIS spectrum obtained on 2022 September 22. At this time, the SN was barely visible in the spectrum, so the slit was positioned to pass through the host-galaxy nucleus and we extracted the spectrum at the nucleus to avoid SN contamination. We derive a redshift for the host galaxy (based on the Hα emission line) of $z = 0.0323 \pm 0.0001$ and a distance of 141.8 Mpc, in agreement with Gutiérrez et al. (2022). SN 2020wnt has a radial offset of 6.″3 from the host-galaxy nucleus, corresponding to a physical offset of 4.3 kpc at the distance of the host.

To derive the host-galaxy properties of SN 2020wnt, we first measure the broadband photometric properties. Due to the irregular nature of the galaxy, we carefully perform elliptical aperture photometry (radius of 7.″9, axis ratio of 0.6, and angle 30° east of north) on Pan-STARRS1 (PS1) images (Chambers et al. 2016). Host photometry is detailed in Table A3. We note that our measured photometry differ from that in the PS1 catalog due primarily to the consistent aperture sizes used in different bands.

We model the host-galaxy SED based on our PS1 photometry using the LE PHARE package (Arnouts et al. 1999; Ilbert et al. 2006), correcting the photometry for Milky Way foreground extinction prior to fitting. The code uses the population-synthesis templates of Bruzual & Charlot (2003), summed according to an exponentially declining burst of star formation and with stellar metallicities between 0.2 $Z_\odot < Z < Z_\odot$ and assuming a Chabrier initial mass function (Chabrier 2003). Dust attenuation in the galaxy is applied to the SED models using the Calzetti et al. (2000) reddening law. We derive a host stellar mass of $\log(M/M_\odot) = 8.81^{+0.09}_{-0.18}$ and an integrated star formation rate (SFR) of $\log(\mathrm{SFR}) = -1.58^{+0.31}_{-0.40}$ $M_\odot$ yr^{-1}, respectively. The values represent best-fit SED and 1σ uncertainties derived from MCMC simulations. The best fit is shown in Figure A1.

This is 0.51 dex higher in stellar mass than in Gutiérrez et al. (2022). However, the photometry used in Gutiérrez et al. (2022) was the catalog PS1 photometry (4.″4 Kron radius for the r band, centered on the nuclear region of the host), which does not encompass all the flux of the galaxy, given the

irregular morphology. When we fit a model SED to this catalog PS1 photometry we derive a a host stellar mass of $\log(M/M_{\odot}) = 8.30^{+0.10}_{-0.11}$ and an integrated SFR of $\log(\mathrm{SFR}) = -2.55^{+0.61}_{-0.38}$ $M_{\odot}$ yr^{-1}, which is consistent with the measurements in Gutiérrez et al. (2022).

We then constrain the spectroscopic properties from our Keck/LRIS spectrum. We corrected the host galaxy photometry for Milky Way reddening (Schlafly & Finkbeiner 2011), and modeled the host-galaxy stellar continuum using the `Firefly` code[24] (Wilkinson et al. 2017) with MaStar Models (Maraston et al. 2020). The stellar continuum model is convolved to the resolution of the spectrum and subtracted to remove the stellar Balmer absorption. The Galactic-reddening-corrected spectrum is plotted in Figure 12, and the stellar continuum is plotted in a tangerine color. Emission-line features are labeled.

We then measure emission-line fluxes from our one-dimensional spectrum by fitting a Gaussian profile for each line of interest. Flux values are available in Table A2. We calculate the Balmer decrement extinction Hα/Hβ to estimate the visual extinction as $A_V = 0.006^{+0.173}_{-0.006}$ mag, assuming the Calzetti et al. (2000) attenuation law.

We plot the host of SN 2020wnt on a Baldwin–Phillips–Telervich diagram (Baldwin et al. 1981; Veilleux & Osterbrock 1987) to check for contamination with an AGN. In the top -right panel of Figure 12 we plot SN 2020wnt alongside other SLSNe from Perley et al. (2016). SN 2020wnt clearly falls on the star-forming main sequence, and shows no evidence for harboring an AGN. We then measured the spectroscopic SFR using the Hα line. We corrected the Hα flux for extinction and used the Hα luminosity with the standard conversion of Kennicutt (1998) to derive a star formation rate of $\log(\mathrm{SFR}_{H\alpha}) = -0.92^{+0.07}_{-0.01}$ $M_{\odot}$ yr^{-1}, which is 0.66 dex higher than the photometric SFR measurement but still consistent within the measurement uncertainties.

In addition, we derived the nuclear metallicity of the host galaxy. We detected the temperature-sensitive [O II] λ4363 auroral oxygen feature (9.9σ), as well as [O II] λ7720, 7730 (7.0, 5.0σ). Thus, we employed a direct method to measure the metallicity. We used the python package `PyNeb v1.1.16` (Luridiana et al. 2015). We assumed a two-zone model for the H II regions, where the high-ionization zone is traced by [O III] and the low-ionization zone is traced by [O II], [N II], and [S II] (e.g., Stasińska 1982). To get from the observed line fluxes to the metallicity, we first corrected all line fluxes for the attenuation in the host galaxy. Afterwards, we computed the electron density from the ratio of the [S II] doublet and the electron temperature of the high-ionization species from the flux ratio between [O III] λ4363 and [O III] λ4959 + [O III] λ5007. The temperature of the low-ionization species is computed with Equation (14) in Izotov et al. (2006) for the intermediate-metallicity case ($12 + \log \mathrm{O/H} \approx 7.6$). With the electron temperatures in hand (Table A2), we can directly infer the oxygen abundance of O^+ and O^{2+} with `PyNeb`: $12 + \log \mathrm{O^+/H} = 7.54^{+0.07}_{-0.06}$ and $12 + \log \mathrm{O^{2+}/H} = 7.91^{+0.06}_{-0.05}$ (Table A2). The total oxygen abundance is $12 + \log \mathrm{O/H} = 8.06 \pm 0.06$. This corresponds to a metallicity of 0.24 ± 0.03 solar, using a solar oxygen abundance of 8.69 (Asplund et al. 2009).

[24] https://github.com/FireflySpectra/firefly_release

The top-left panel of Figure 12 shows a mass–metallicity diagram. SN 2020wnt is consistent with other SLSNe-I. It has a slightly lower metallicity (0.14 dex) than the average metallicity of SLSNe-I host galaxies ($12 + \log \mathrm{O/H} \approx 8.2$; Leloudas et al. 2015; Perley et al. 2016) and the stellar mass is higher (0.91 dex) than the average stellar mass of other low-redshift SLSNe-I host galaxies ($\log(M/M_{\odot}) \approx 7.9$; Perley et al. 2016; Schulze et al. 2021; Taggart & Perley 2021).

9. Summary

SN 2020wnt presents one of the best views yet of a rare death of a very massive star. From the optical and near-IR observations we present in this paper, we find the following:

1. The light curve of SN 2020wnt consists of a ~5 days long early-time bump, a diffusive peak, and a nebular decline with a 1 mag dip around 200 days post peak. The early bump is likely caused by the presence of a compact CSM ejected immediately before the explosion, possibly by nuclear burning instability. The shock cooling from the interactions between this CSM and the SN shock results in the emission we observe. The diffusive peak appears similar to a light curve of SNe Ibc and not that of SLSNe I. Lastly, the nebular decline is consistent with several models considered. The dip is most likely due to dust formation. The rise time of the bolometric light curve is 69 ± 2 days to a peak luminosity of $(6.8 \pm 0.3) \times 10^{43}$ erg s^{-1}.
2. The optical spectra of SN 2020wnt prior to 100 days post peak are quantitatively similar to those of SNe Ic and not magnetar-powered SLSNe I (Figures 6 and 7). The blue continuum and O II absorption lines, associated with magnetar heating, are not present. However, late-time spectra much better resemble the mean SLSN I late-time spectrum rather than the mean SN Ic spectrum. Spectroscopic signatures attributed to a central engine in SLSNe I are visible in SN 2020wnt's spectra at these epochs: enhanced blue flux, an emission feature at 5000 Å associated with [Fe II] and [O III], and narrow O I recombination lines. This spectral evolution suggests that a central engine may be operating in SN 2020wnt, but is not visible until later in the nebular phase.
3. The extensive near-IR spectroscopic data of SN 2020wnt reveal features not captured in the optical. The most notable is the emerging CO emission at 2.3 μm starting at 241 days post peak and the rising dust continuum. These observations support our conclusion that the dip in the optical light curves around 200 days post peak is due to additional dust absorption. SN 2020wnt is the first SLSN with a CO detection, thanks to its low redshift allowing for the observation of the 2.3 μm band from the ground. It is also the second SLSN with an observation of dust continuum (after SN 2018bsz; Chen et al. 2021). This finding highlights the need for space-based IR observations of SLSNe with JWST.
4. Our light-curve modeling effort disfavors a PISN as the explosion mechanism responsible for SN 2020wnt. The predicted light curves evolve too slowly and it is not possible to reproduce both the rise time and the peak luminosity. The large ^{56}Ni mass that would be required to power the peak of SN 2020wnt is simply too large to synthesize without a PI explosion. We instead favor

magnetar models, with a large enough total ejecta mass to hide the spectroscopic effects from magnetar heating until later in the evolution. The T50 model from Table 1 is our preferred model.

5. Our nebular spectra comparison also disfavors the PI model (Figure 11) due to the lack of strong intermediate-mass element lines predicted. The nebular spectra comparison to a more generic model grid shows that the ejecta of SN 2020wnt are likely very clumpy, suggesting the presence of a central engine.

SN 2020wnt demonstrates the rich and diverse observational properties of a magnetar-powered explosion. Dust and molecule formation remain poorly probed; it would require future JWST observations of these objects, especially at low redshift, to create the first sample of SLSNe with rest-frame IR spectra and to map the chemical evolution of SLSN ejecta. More importantly, it seems that peak optical spectra may not necessarily reveal all explosions that harbor a magnetar. SN 2020wnt shows us that the spectroscopic signatures related to a central engine may be hidden near peak in events with large ejecta mass and lower-energy magnetars. Nebular spectroscopy of luminous SNe that have SNe Ibc-like spectra at peak is needed to constrain the fraction of SESNe harboring a central engine. It could very well be possible that all SESNe (or even hydrogen-rich CCSNe) are affected by the neutron star formed in core collapse to a different degree, and that that there is a continuum between "normal" and "superluminous" SNe. Late-time observations, both photometric and spectroscopic, with near-IR coverage to measure a realistic bolometric luminosity are needed for a large sample of these explosion to measure the distribution of the initial rotation and the magnetic field of a neutron star born out of the core-collapse process.

Acknowledgments

We thank Norbert Langer, Matt Nicholl, Conor Omand, Dan Kasen, David Khatami, Anders Jerkstrand, and Heloise Stevance for helpful discussions. We also thank the organizers of the IAU360 Massive Stars Near and Far symposium, where a lot of helpful discussions about this object were made. We thank Robert Quimby for providing data points used to make Figure 6. We thank Matt Nicholl for providing the mean SLSN and SN Ic spectra for Figure 7. S.S. acknowledges support from the G.R.E.A.T research environment, funded by Vetenskapsrådet, the Swedish Research Council, under project number 2016-06012. A.G. acknowledges support from the Flatiron Institute Center for Computational Astrophysics Pre-Doctoral Fellowship Program in Spring 2022. A.G. is also supported by the Illinois Distinguished Fellowship, the National Science Foundation Graduate Research Fellowship Program under grant No. DGE1746047, and the Center for Astrophysical Surveys Graduate Fellowship at the University of Illinois. Some of the data presented herein were obtained at the W. M. Keck Observatory, which is operated as a scientific partnership among the California Institute of Technology, the University of California and the National Aeronautics and Space Administration. The Observatory was made possible by the generous financial support of the W. M. Keck Foundation. NIRES data presented in this paper were supported in part by NASA Keck PI Data Awards 2020B_N141 and 2021A_N147 (PI: Jha), administered by the NASA Exoplanet Science Institute. Parts of this work are based on observations obtained at the international Gemini Observatory, a program of the NSF's NOIRLab, which is managed by the Association of Universities for Research in Astronomy (AURA) under a cooperative agreement with the National Science Foundation on behalf of the Gemini Observatory partnership: the National Science Foundation (United States), National Research Council (Canada), Agencia Nacional de Investigación y Desarrollo (Chile), Ministerio de Ciencia, Tecnología e Innovación (Argentina), Ministério da Ciência, Tecnologia, Inovações e Comunicações (Brazil), and Korea Astronomy and Space Science Institute (Republic of Korea). This work uses data from the Infrared Telescope Facility, which is operated by the University of Hawaii under contract 80HQTR19D0030 with the National Aeronautics and Space Administration. The authors wish to recognize and acknowledge the very significant cultural role and reverence that the summit of Maunakea has always had within the indigenous Hawaiian community. We are most fortunate to have the opportunity to conduct observations from this mountain. Parts of this work are based on observations obtained with the Samuel Oschin Telescope 48 inch and the 60 inch Telescope at the Palomar Observatory as part of the Zwicky Transient Facility project. ZTF is supported by the National Science Foundation under grant Nos. AST-1440341 and AST-2034437 and a collaboration including current partners Caltech, IPAC, the Weizmann Institute of Science, the Oskar Klein Center at Stockholm University, the University of Maryland, Deutsches Elektronen-Synchrotron and Humboldt University, the TANGO Consortium of Taiwan, the University of Wisconsin at Milwaukee, Trinity College Dublin, Lawrence Livermore National Laboratories, IN2P3, University of Warwick, Ruhr University Bochum, Northwestern University and former partners the University of Washington, Los Alamos National Laboratories, and Lawrence Berkeley National Laboratories. Operations are conducted by COO, IPAC, and UW. The ZTF forced-photometry service was funded under the Heising-Simons Foundation grant No. 12540303 (PI: Graham). Parts of this work are based on observations made with the Nordic Optical Telescope, owned in collaboration by the University of Turku and Aarhus University, and operated jointly by Aarhus University, the University of Turku and the University of Oslo, representing Denmark, Finland and Norway, the University of Iceland, and Stockholm University at the Observatorio del Roque de los Muchachos, La Palma, Spain, of the Instituto de Astrofisica de Canarias.

Software: YSE-PZ (Coulter et al. 2022), CASA (McMullin et al. 2007), spextool (Cushing et al. 2004), xtellcor (Vacca et al. 2003), IRAF (Tody 1986, 1993), george (Ambikasaran et al. 2015), LE PHARE package (Arnouts et al. 1999; Ilbert et al. 2006), PyNeb (v1.1.16; Luridiana et al. 2015), KEPLER (Weaver et al. 1978; Woosley et al. 2002; Woosley 2017), Firefly (Wilkinson et al. 2017).

Appendix

We list all spectroscopic observations in Table A1. We show spectral properties of the host galaxy of SN 2020wnt in Table A2 and host galaxy photometry in Table A3. We show the velocity and composition plots for the models C100 and T50 in Figure A1, left and right, respectively. We plot light curve models He20, T50, and T70 in Figure A2 left, middle, and right, respectively, with contributions from the magnetar, radioactive decay, and CSM plotted separately. We compare the nebular spectrum of SN 2020wnt with the best-fit model from Jerkstrand et al. (2017) and one from Dessart (2019) in Figure A3. Lastly, we plot the best fit SED of the host galaxy of SN 2020wnt in Figure A4.

Table A1
Log of Spectroscopic Observations

Date (UT)	MJD	Days from Peak	Telescope/Instrument
		Optical	
2020-11-11	59164	−47	P200/DBSP
2020-11-15	59168	−43	Shane/Kast
2020-12-06	59189	−23	NOT/ALFOSC
2020-12-14	59197	−15	NOT/ALFOSC
2020-12-22	59205	−7	Shane/Kast
2021-01-06	59220	6	Shane/Kast
2021-01-07	59221	7	P200/DBSP
2021-01-11	59225	11	Shane/Kast
2021-01-20	59234	20	NOT/ALFOSC
2021-02-06	59251	36	Shane/Kast
2021-02-11	59256	41	Shane/Kast
2021-02-19	59264	49	Shane/Kast
2021-03-22	59295	79	Shane/Kast
2021-04-06	59310	93	Shane/Kast
2021-07-15	59410	190	P200/DBSP
2021-07-15	59410	190	Shane/Kast
2021-07-28	59423	203	NOT/ALFOSC
2021-08-03	59429	209	Shane/Kast
2021-08-06	59432	212	Keck/LRIS
2021-08-12	59438	217	Keck/LRIS
2021-08-13	59439	218	Shane/Kast
2021-09-04	59461	240	Keck/LRIS
2021-11-06	59524	301	Keck/LRIS
2022-01-05	59584	359	Keck/LRIS
2022-09-22	59844	611	Keck/LRIS
		Near-infrared	
2020-12-24	59207	−5	Keck/NIRES
2021-02-04	59249	34	P200/TSpec
2021-02-22	59267	52	IRTF/SpeX
2021-02-23	59268	53	Keck/NIRES
2021-03-24	59297	81	Gemini/GNIRS
2021-09-05	59462	241	IRTF/SpeX
2021-11-19	59537	313	Gemini/GNIRS
2022-01-25	59604	379	HST/WFC3

Table A2
Emission-line Measurements and Derived Spectral Properties of the Nucleus of the Host Galaxy of SN 2020wnt

Measurement	Unit/Wavelength	Value
A_V	mag	$0.006^{+0.173}_{-0.006}$
SFR Hα	$M_\odot$ yr^{-1}	$0.075^{+0.014}_{-0.001}$
T_e([O II])	K	11991^{+388}_{-415}
T_e([O III])	K	12184^{+472}_{-471}
12+log$_{10}$(O+/H+)		$7.54^{+0.07}_{-0.06}$
12+log$_{10}$(O++/H+)		$7.91^{+0.06}_{-0.05}$
12+log$_{10}$(O/H)		8.06 ± 0.06
Z	$Z_\odot$	0.24 ± 0.03
Hα	6563	389.9 ± 2.8
Hβ	4861	136.1 ± 5.7
Hγ	4340	62.3 ± 3.2
[O II]	3727	260.0 ± 11.5
[O III]	4363	6.9 ± 0.7
[O III]	4959	200.6 ± 4.6
[O III]	5007	582.7 ± 19.4
[N II]	6548	5.8 ± 1.8
[N II]	6584	14.6 ± 2.1
[S II]	6716	36.3 ± 0.4
[S II]	6731	25.8 ± 1.7
[O II]	7320	3.5 ± 0.5
[O II]	7330	4.0 ± 0.8
[S III]	9069	27.5 ± 0.5
[S III]	9531	50.8 ± 0.7

Notes. The Balmer decrement is calculated assuming the Calzetti et al. (2000) extinction law. The SFR is derived using the Kennicutt (1998) relation. All emission lines fluxes are corrected for Galactic foreground extinction (Schlafly & Finkbeiner 2011), but are not corrected for the internal attenuation within the host system. Line flux values are in units of 10^{-17} erg cm^{-2} s^{-1}Å^{-1} and uncertainties are 1σ.

Table A3
Photometry of SN 2020wnt's Host Galaxy

Filter	Magnitude	Instrument	Reference
g	19.35 ± 0.12	PS1	This work
r	18.67 ± 0.10	PS1	This work
i	18.38 ± 0.11	PS1	This work
z	18.22 ± 0.11	PS1	This work
y	18.05 ± 0.25	PS1	This work

Note. Magnitudes are not corrected for Galactic foreground extinction.

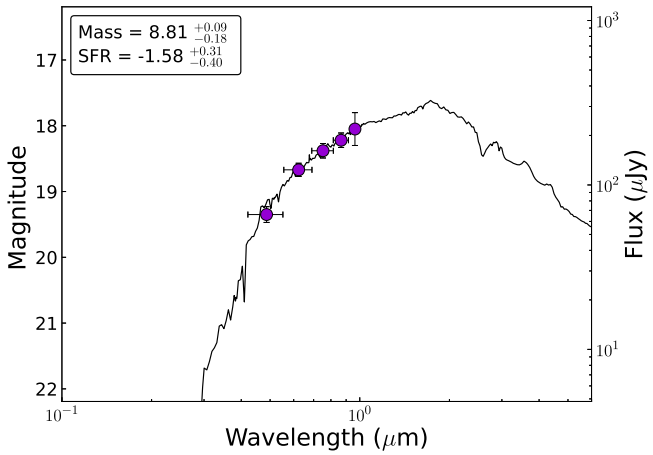

Figure A1. Fit to the spectral energy distribution (SED) of the host of 2020wnt using the SED modeling code `Le Phare` (Ilbert et al. 2006). Observed PS1 photometry is plotted in purple.

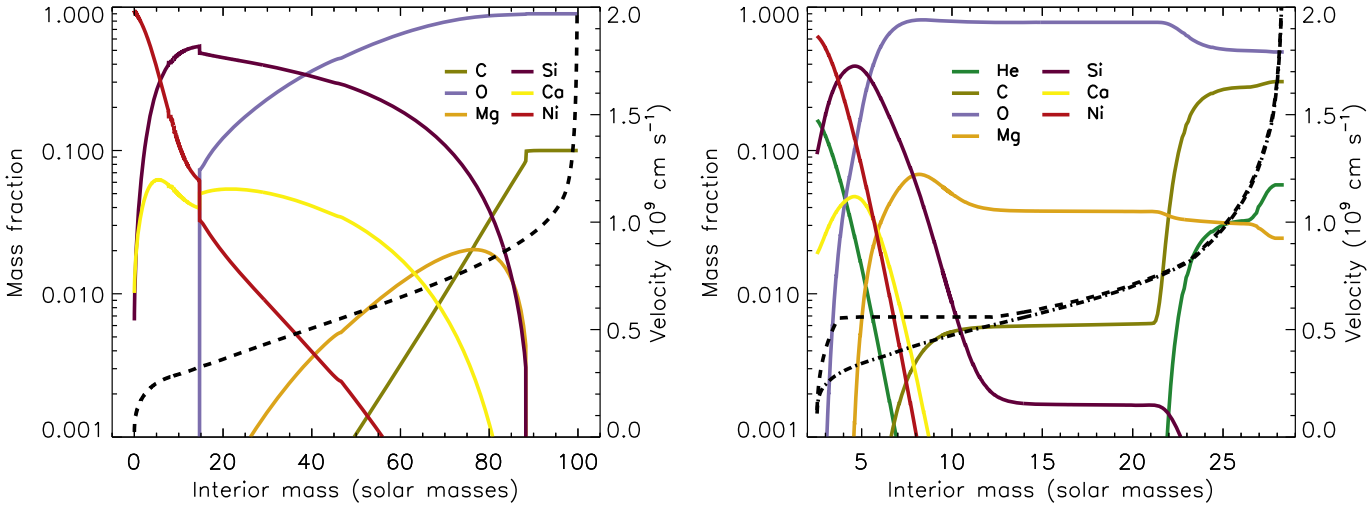

Figure A2. Left: velocity (dashed line) and composition of Model C100 (Table 1). The explosion energy was 4.37 × 10^{52} erg and 5.13 $M_\odot$ of ^{56}Ni was synthesized. These velocities are not dissimilar to SN 2020wnt. Right: composition and velocity of the Model T50 (Table 1). The dotted–dashed line and the dashed line are the velocity profiles of the ejecta without and with the magnetar, respectively. Note the nearly constant velocity with the magnetar in the inner 11 $M_\odot$, which is a consequence of the pulsar bubble sweeping up matter into a thin shell. A moderate amount of mixing has been artificially applied to the composition.

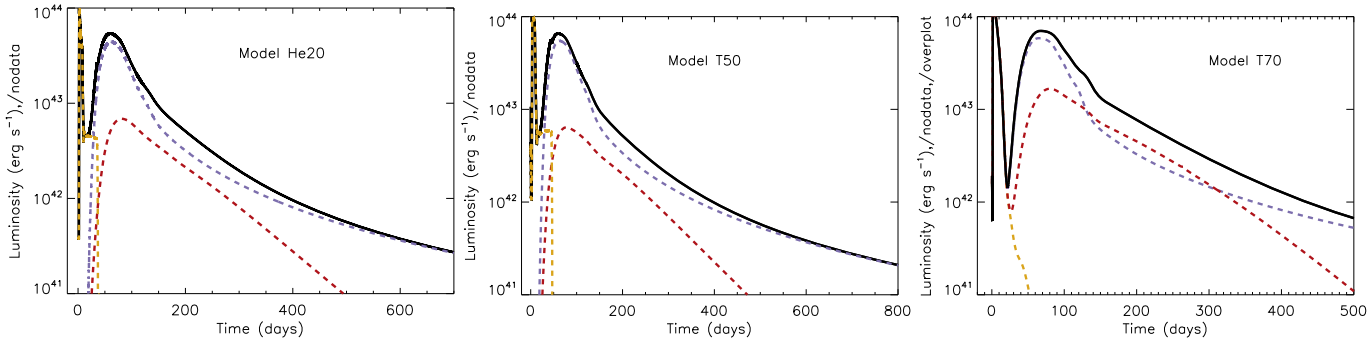

Figure A3. Light curves from models He20, T50, and T70 showing the total luminosity in black, the magnetar contribution in blue, radioactive decay contribution in red, and CSM interaction in orange. The decay power contributes around 10% of the total luminosity in the He20 and T50 models, but nevertheless affects the shape of the light curve. The decay power is significant in the T70 model due to the large ^{56}Ni mass. The brief peak close to explosion in all models is due to either interaction with or breakout from the CSM.

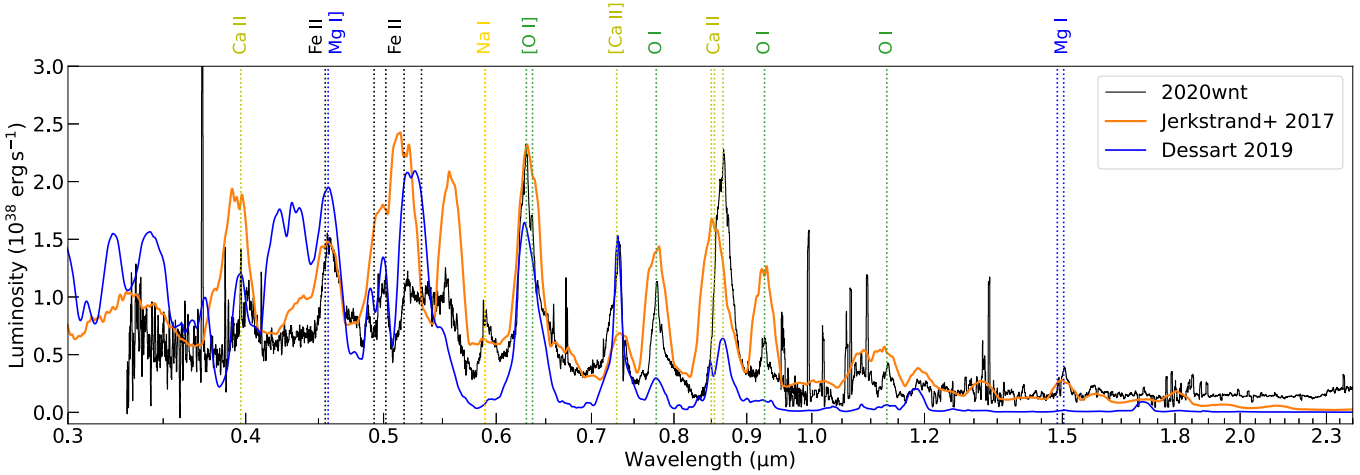

Figure A4. Comparison between the nebular spectrum of SN 2020wnt from 301 to 313 days post peak and model spectra. The best-fit model from Jerkstrand et al. (2017), discussed in Section 7, is shown in orange, while the r0e2cl model from Dessart (2019) is shown in blue. The first model is the same as the bottom panel of Figure 10.

ORCID iDs

Samaporn Tinyanont https://orcid.org/0000-0002-1481-4676
Stan E. Woosley https://orcid.org/0000-0002-3352-7437
Kirsty Taggart https://orcid.org/0000-0002-5748-4558
Ryan J. Foley https://orcid.org/0000-0002-2445-5275
Lin Yan https://orcid.org/0000-0003-1710-9339
Ragnhild Lunnan https://orcid.org/0000-0001-9454-4639
Kyle W. Davis https://orcid.org/0000-0002-5680-4660
Charles D. Kilpatrick https://orcid.org/0000-0002-5740-7747
Matthew R. Siebert https://orcid.org/0000-0003-2445-3891
Steve Schulze https://orcid.org/0000-0001-6797-1889
Chris Ashall https://orcid.org/0000-0002-5221-7557
Ting-Wan Chen https://orcid.org/0000-0002-1066-6098
Kishalay De https://orcid.org/0000-0002-8989-0542
Georgios Dimitriadis https://orcid.org/0000-0001-9494-179X
Dillon Z. Dong https://orcid.org/0000-0001-9584-2531
Christoffer Fremling https://orcid.org/0000-0002-4223-103X
Alexander Gagliano https://orcid.org/0000-0003-4906-8447
Saurabh W. Jha https://orcid.org/0000-0001-8738-6011
David O. Jones https://orcid.org/0000-0002-6230-0151
Mansi M. Kasliwal https://orcid.org/0000-0002-5619-4938
Hao-Yu Miao https://orcid.org/0000-0003-2736-5977
Yen-Chen Pan https://orcid.org/0000-0001-8415-6720
Daniel A. Perley https://orcid.org/0000-0001-8472-1996
Vikram Ravi https://orcid.org/0000-0002-7252-5485
César Rojas-Bravo https://orcid.org/0000-0002-7559-315X
Itai Sfaradi https://orcid.org/0000-0003-0466-3779
Jesper Sollerman https://orcid.org/0000-0003-1546-6615
Vanessa Alarcon https://orcid.org/0000-0001-5485-1570
Rodrigo Angulo https://orcid.org/0000-0001-5281-731X
Karoli E. Clever https://orcid.org/0000-0001-8756-1262
Cirilla Couch https://orcid.org/0000-0002-4653-9015
Srujan Dandu https://orcid.org/0000-0003-4578-3216
Atirath Dhara https://orcid.org/0000-0002-5950-1702
Zhisen Lai https://orcid.org/0000-0001-8483-9089

References

Afsariardchi, N., Drout, M. R., Khatami, D. K., et al. 2021, ApJ, 918, 89
Aguilera-Dena, D. R., Langer, N., Moriya, T. J., & Schootemeijer, A. 2018, ApJ, 858, 115
Ambikasaran, S., Foreman-Mackey, D., Greengard, L., Hogg, D. W., & O'Neil, M. 2015, ITPAM, 38, 252
Anderson, J. P., Pessi, P. J., Dessart, L., et al. 2018, A&A, 620, A67
Angus, C. R., Smith, M., Sullivan, M., et al. 2019, MNRAS, 487, 2215
Arnett, W. D. 1982, ApJ, 253, 785
Arnouts, S., Cristiani, S., Moscardini, L., et al. 1999, MNRAS, 310, 540
Asplund, M., Grevesse, N., Sauval, A. J., & Scott, P. 2009, ARA&A, 47, 481
Baldwin, J. A., Phillips, M. M., & Terlevich, R. 1981, PASP, 93, 5
Barbary, K., Dawson, K. S., Tokita, K., et al. 2009, ApJ, 690, 1358
Barkat, Z., Rakavy, G., & Sack, N. 1967, PhRvL, 18, 379
Barlow, M. J., Krause, O., Swinyard, B. M., et al. 2010, A&A, 518, L138
Becker, A. 2015, HOTPANTS: High Order Transform of PSF ANd Template Subtraction, Astrophysics Source Code Library, record ascl:1504.004
Bellm, E. C., Kulkarni, S. R., Graham, M. J., et al. 2019, PASP, 131, 018002
Ben-Ami, S., Gal-Yam, A., Mazzali, P. A., et al. 2014, ApJ, 785, 37
Bersten, M. C., Benvenuto, O. G., Nomoto, K., et al. 2012, ApJ, 757, 31
Blondin, S., Matheson, T., Kirshner, R. P., et al. 2012, AJ, 143, 126
Branch, D., Benetti, S., Kasen, D., et al. 2002, ApJ, 566, 1005
Bruzual, G., & Charlot, S. 2003, MNRAS, 344, 1000
Calzetti, D., Armus, L., Bohlin, R. C., et al. 2000, ApJ, 533, 682
Cardelli, J. A., Clayton, G. C., & Mathis, J. S. 1989, ApJ, 345, 245
Chabrier, G. 2003, PASP, 115, 763
Chambers, K. C., Magnier, E. A., Metcalfe, N., et al. 2016, arXiv:1612.05560
Chandra, P. 2018, SSRv, 214, 27
Chatzopoulos, E., van Rossum, D. R., Craig, W. J., et al. 2015, ApJ, 799, 18
Chatzopoulos, E., Wheeler, J. C., & Couch, S. M. 2013, ApJ, 776, 129
Chen, K.-J., Woosley, S., Heger, A., Almgren, A., & Whalen, D. J. 2014, ApJ, 792, 28
Chen, K.-J., Woosley, S. E., & Sukhbold, T. 2016, ApJ, 832, 73
Chen, T. W., Brennan, S. J., Wesson, R., et al. 2021, arXiv:2109.07942
Chen, T. W., Inserra, C., Fraser, M., et al. 2018, ApJL, 867, L31
Chen, T. W., Smartt, S. J., Jerkstrand, A., et al. 2015, MNRAS, 452, 1567
Chen, Z. H., Yan, L., Kangas, T., et al. 2023a, ApJ, 943, 42
Chen, Z. H., Yan, L., Kangas, T., et al. 2023b, ApJ, 943, 41
Chevalier, R. A. 1998, ApJ, 499, 810
Chevalier, R. A., & Irwin, C. M. 2011, ApJL, 729, L6
Chomiuk, L., Chornock, R., Soderberg, A. M., et al. 2011, ApJ, 743, 114
Coulter, D. A., Jones, D. O., McGill, P., et al. 2022, YSE-PZ: An Open-source Target and Observation Management System, v0.3.0, Zenodo, doi:10.5281/zenodo.7278430
Cushing, M. C., Vacca, W. D., & Rayner, J. T. 2004, PASP, 116, 362
Davis, S., Hsiao, E. Y., Ashall, C., et al. 2019, ApJ, 887, 4
De, K., Hankins, M. J., Kasliwal, M. M., et al. 2020, PASP, 132, 025001
de Mink, S. E., Langer, N., Izzard, R. G., Sana, H., & de Koter, A. 2013, ApJ, 764, 166
Dessart, L. 2019, A&A, 621, A141
Dessart, L., Hillier, D. J., Waldman, R., Livne, E., & Blondin, S. 2012, MNRAS, 426, L76
Dexter, J., & Kasen, D. 2013, ApJ, 772, 30
Dwek, E., & Arendt, R. G. 2015, ApJ, 810, 75
Elias, J. H., Joyce, R. R., Liang, M., et al. 2006a, Proc. SPIE, 6269, 62694C
Elias, J. H., Rodgers, B., Joyce, R. R., et al. 2006b, Proc. SPIE, 6269, 626914
Ertl, T., Woosley, S. E., Sukhbold, T., & Janka, H. T. 2020, ApJ, 890, 51
Fiore, A., Chen, T. W., Jerkstrand, A., et al. 2021, MNRAS, 502, 2120
Fitzpatrick, E. L. 1999, PASP, 111, 63
Flewelling, H. A., Magnier, E. A., Chambers, K. C., et al. 2020, ApJS, 251, 7
Foreman-Mackey, D., Hogg, D. W., Lang, D., & Goodman, J. 2013, PASP, 125, 306
Förster, F., Bauer, F. E., Munoz-Arancibia, A., et al. 2020, TNSTR, 2020-3110, 1
Förster, F., Cabrera-Vives, G., Castillo-Navarrete, E., et al. 2021, AJ, 161, 242
Fox, O. D., Chevalier, R. A., Skrutskie, M. F., et al. 2011, ApJ, 741, 7
Fox, O. D., Filippenko, A. V., Skrutskie, M. F., et al. 2013, AJ, 146, 2
Fuller, J., & Ro, S. 2018, MNRAS, 476, 1853
Gagliano, A., Izzo, L., Kilpatrick, C. D., et al. 2022, ApJ, 924, 55
Galama, T. J., Vreeswijk, P. M., van Paradijs, J., et al. 1998, Natur, 395, 670
Gall, C., & Hjorth, J. 2018, ApJ, 868, 62
Gall, C., Hjorth, J., & Andersen, A. C. 2011, A&ARv, 19, 43
Gal-Yam, A. 2012, Sci., 337, 927
Gal-Yam, A. 2019, ARA&A, 57, 305
Gal-Yam, A., Mazzali, P., Ofek, E. O., et al. 2009, Natur, 462, 624
Gehrels, N., Chincarini, G., Giommi, P., et al. 2004, ApJ, 611, 1005
Gerardy, C. L., Fesen, R. A., Nomoto, K., et al. 2002, PASJ, 54, 905
Gilmer, M. S., Kozyreva, A., Hirschi, R., Fröhlich, C., & Yusof, N. 2017, ApJ, 846, 100
Gomez, S., Berger, E., Hosseinzadeh, G., et al. 2021, ApJ, 913, 143
Gomez, S., Berger, E., Nicholl, M., Blanchard, P. K., & Hosseinzadeh, G. 2022, ApJ, 941, 107
Graham, M. J., Kulkarni, S. R., Bellm, E. C., et al. 2019, PASP, 131, 078001
Gutiérrez, C. P., Pastorello, A., Bersten, M., et al. 2022, MNRAS, 517, 2056
Heger, A., & Woosley, S. E. 2002, ApJ, 567, 532
Herter, T. L., Henderson, C. P., Wilson, J. C., et al. 2008, Proc. SPIE, 7014, 70140X
Horne, K. 1986, PASP, 98, 609
Hosseinzadeh, G., Berger, E., Metzger, B. D., et al. 2022, ApJ, 933, 14
Howell, D. A., Sullivan, M., Nugent, P. E., et al. 2006, Natur, 443, 308
Hsiao, E. Y., Phillips, M. M., Marion, G. H., et al. 2019, PASP, 131, 014002
Hunter, D. J., Valenti, S., Kotak, R., et al. 2009, A&A, 508, 371
Ilbert, O., Arnouts, S., McCracken, H. J., et al. 2006, A&A, 457, 841
Indebetouw, R., Matsuura, M., Dwek, E., et al. 2014, ApJL, 782, L2
Inserra, C., Nicholl, M., Chen, T. W., et al. 2017, MNRAS, 468, 4642h
Inserra, C., Smartt, S. J., Gall, E. E. E., et al. 2018, MNRAS, 475, 1046
Inserra, C., Smartt, S. J., Jerkstrand, A., et al. 2013, ApJ, 770, 128
Izotov, Y. I., Stasińska, G., Meynet, G., Guseva, N. G., & Thuan, T. X. 2006, A&A, 448, 955
Jerkstrand, A., Smartt, S. J., & Heger, A. 2016, MNRAS, 455, 3207
Jerkstrand, A., Smartt, S. J., Inserra, C., et al. 2017, ApJ, 835, 13

Kasen, D., & Bildsten, L. 2010, ApJ, 717, 245
Kasen, D., Metzger, B. D., & Bildsten, L. 2016, ApJ, 821, 36
Kasen, D., Woosley, S. E., & Heger, A. 2011, ApJ, 734, 102
Kennicutt, R. C. J. 1998, ARA&A, 36, 189
Khatami, D. K., & Kasen, D. N. 2019, ApJ, 878, 56
Kozyreva, A., & Blinnikov, S. 2015, MNRAS, 454, 4357
Kozyreva, A., Gilmer, M., Hirschi, R., et al. 2017, MNRAS, 464, 2854
Lang, D. 2014, AJ, 147, 108
Lau, R. M., Hankins, M. J., Kasliwal, M. M., et al. 2021, ApJ, 909, 113
Lau, R. M., Herter, T. L., Morris, M. R., Li, Z., & Adams, J. D. 2015, Sci., 348, 413
Leloudas, G., Chatzopoulos, E., Dilday, B., et al. 2012, A&A, 541, A129
Leloudas, G., Schulze, S., Krühler, T., et al. 2015, MNRAS, 449, 917
Leung, S.-C., Wu, S., & Fuller, J. 2021, ApJ, 923, 41
Li, J.-Y., Wang, S.-Q., Gan, W.-P., et al. 2022, ApJ, 928, 77
Liu, Y.-Q., Modjaz, M., Bianco, F. B., & Graur, O. 2016, ApJ, 827, 90
Lunnan, R., Chornock, R., Berger, E., et al. 2016, ApJ, 831, 144
Lunnan, R., Chornock, R., Berger, E., et al. 2018, ApJ, 852, 81
Luridiana, V., Morisset, C., & Shaw, R. A. 2015, A&A, 573, A42
Lyman, J. D., Bersier, D., James, P. A., et al. 2016, MNRAS, 457, 328
MacFadyen, A. I., & Woosley, S. E. 1999, ApJ, 524, 262
MacFadyen, A. I., Woosley, S. E., & Heger, A. 2001, ApJ, 550, 410
Mainzer, A., Bauer, J., Cutri, R. M., et al. 2014, ApJ, 792, 30
Maraston, C., Hill, L., Thomas, D., et al. 2020, MNRAS, 496, 2962
Marchant, P., Renzo, M., Farmer, R., et al. 2019, ApJ, 882, 36
Masci, F. J., Laher, R. R., Rusholme, B., et al. 2019, PASP, 131, 018003
Matsuura, M., Dwek, E., Barlow, M. J., et al. 2015, ApJ, 800, 50
Mazzali, P. A., Moriya, T. J., Tanaka, M., & Woosley, S. E. 2019, MNRAS, 484, 3451
Mazzali, P. A., Sullivan, M., Pian, E., Greiner, J., & Kann, D. A. 2016, MNRAS, 458, 3455
McMullin, J. P., Waters, B., Schiebel, D., Young, W., & Golap, K. 2007, in ASP Ser. 376, Astronomical Data Analysis Software and Systems XVI, ed. R. A. Shaw, F. Hill, & D. J. Bell (San Francisco, CA: ASP), 127
Meisner, A. M., Lang, D., & Schlegel, D. J. 2018, AJ, 156, 69
Metzger, B. D., Margalit, B., Kasen, D., & Quataert, E. 2015, MNRAS, 454, 3311
Rodríguez, Ó., Meza, N., Pineda-García, J., & Ramirez, M. 2021, MNRAS, 505, 1742
Miller, J. S., & Stone, R. P. S. 1993, LOTRM
Milligan, S., Cranton, B. W., & Skrutskie, M. F. 1996, Proc. SPIE, 2863, 2
Modjaz, M., Liu, Y. Q., Bianco, F. B., & Graur, O. 2016, ApJ, 832, 108
Moriya, T. J., Mazzali, P. A., & Tanaka, M. 2019, MNRAS, 484, 3443
Moriya, T. J., Nicholl, M., & Guillochon, J. 2018, ApJ, 867, 113
Nicholl, M. 2018, RNAAS, 2, 230
Nicholl, M. 2021, A&G, 62, 5.34
Nicholl, M., Berger, E., Blanchard, P. K., Gomez, S., & Chornock, R. 2019, ApJ, 871, 102
Nicholl, M., Berger, E., Smartt, S. J., et al. 2016a, ApJ, 826, 39
Nicholl, M., Berger, E., Margutti, R., et al. 2016b, ApJL, 828, L18
Nicholl, M., Guillochon, J., & Berger, E. 2017, ApJ, 850, 55
Nicholl, M., & Smartt, S. J. 2016, MNRAS, 457, L79
Nicholl, M., Smartt, S. J., Jerkstrand, A., et al. 2013, Natur, 502, 346
Nicholl, M., Smartt, S. J., Jerkstrand, A., et al. 2014, MNRAS, 444, 2096
Nicholl, M., Smartt, S. J., Jerkstrand, A., et al. 2015, ApJL, 807, L18
Nieuwenhuijzen, H., & de Jager, C. 1990, A&A, 231, 134
Ofek, E. O., Cameron, P. B., Kasliwal, M. M., et al. 2007, ApJL, 659, L13
Oke, J. B., Cohen, J. G., Carr, M., et al. 1995, PASP, 107, 375
Oke, J. B., & Gunn, J. E. 1982, PASP, 94, 586
Omand, C. M. B., Kashiyama, K., & Murase, K. 2019, MNRAS, 484, 5468
Ostriker, J. P., & Gunn, J. E. 1971, ApJL, 164, L95
Perley, D. A., Quimby, R. M., Yan, L., et al. 2016, ApJ, 830, 13
Piro, A. L. 2015, ApJL, 808, L51
Piro, A. L., Haynie, A., & Yao, Y. 2021, ApJ, 909, 209
Pursiainen, M., Leloudas, G., Paraskeva, E., et al. 2022, A&A, 666, A30
Quimby, R. M., Aldering, G., Wheeler, J. C., et al. 2007, ApJL, 668, L99
Quimby, R. M., De Cia, A., Gal-Yam, A., et al. 2018, ApJ, 855, 2
Quimby, R. M., Kulkarni, S. R., Kasliwal, M. M., et al. 2011, Natur, 474, 487
Rakavy, G., & Shaviv, G. 1967, ApJ, 148, 803
Rayner, J. T., Toomey, D. W., Onaka, P. M., et al. 2003, PASP, 115, 362
Rest, A., Stubbs, C., Becker, A. C., et al. 2005, ApJ, 634, 1103
Rho, J., Evans, A., Geballe, T. R., et al. 2021, ApJ, 908, 232
Rho, J., Geballe, T. R., Banerjee, D. P. K., et al. 2018a, ApJL, 864, L20
Rho, J., Gomez, H. L., Boogert, A., et al. 2018b, MNRAS, 479, 5101
Rho, J., Kozasa, T., Reach, W. T., et al. 2008, ApJ, 673, 271
Rho, J., Reach, W. T., Tappe, A., et al. 2009, ApJ, 700, 579
Roming, P. W. A., Kennedy, T. E., Mason, K. O., et al. 2005, SSRv, 120, 95
Sarangi, A., & Cherchneff, I. 2015, A&A, 575, A95
Sarangi, A., Matsuura, M., & Micelotta, E. R. 2018, SSRv, 214, 63
Schechter, P. L., Mateo, M., & Saha, A. 1993, PASP, 105, 1342
Schlafly, E. F., & Finkbeiner, D. P. 2011, ApJ, 737, 103
Schulze, S., Yaron, O., Sollerman, J., et al. 2021, ApJS, 255, 29
Shahbandeh, M., Hsiao, E. Y., Ashall, C., et al. 2022, ApJ, 925, 175
Shiode, J. H., & Quataert, E. 2014, ApJ, 780, 96
Skrutskie, M. F., Cutri, R. M., Stiening, R., et al. 2006, AJ, 131, 1163
Smith, K. W., Smartt, S. J., Young, D. R., et al. 2020, PASP, 132, 085002
Smith, M., Sullivan, M., D'Andrea, C. B., et al. 2016, ApJL, 818, L8
Smith, N. 2017, in Handbook of Supernovae, ed. A. Alsabti & P. Murdin (Cham: Springer), 403
Smith, N., Li, W., Foley, R. J., et al. 2007, ApJ, 666, 1116
Sollerman, J., Holland, S. T., Challis, P., et al. 2002, A&A, 386, 944
Sollerman, J., Yang, S., Perley, D., et al. 2022, A&A, 657, A64
Spyromilio, J., Meikle, W. P. S., Learner, R. C. M., & Allen, D. A. 1988, Natur, 334, 327
Sravan, N., Marchant, P., Kalogera, V., Milisavljevic, D., & Margutti, R. 2020, ApJ, 903, 70
Stasińska, G. 1982, A&AS, 48, 299
Sun, L., Xiao, L., & Li, G. 2022, MNRAS, 513, 4057
Szalai, T., & Vinkó, J. 2013, A&A, 549, A79
Szalai, T., Zsíros, S., Fox, O. D., Pejcha, O., & Müller, T. 2019, ApJS, 241, 38
Taddia, F., Fremling, C., Sollerman, J., et al. 2016, A&A, 592, A89
Taddia, F., Sollerman, J., Fremling, C., et al. 2019, A&A, 621, A64
Taggart, K., & Perley, D. A. 2021, MNRAS, 503, 3931
Tinyanont, S. 2022, Supernova 2020wnt: An Atypical Superluminous Supernova with a Hidden Central Engine, MAST, doi:10.17909/hg36-3f30
Tinyanont, S., Dimitriadis, G., & Foley, R. J. 2020, TNSCR, 2020-3473, 1
Tinyanont, S., Kasliwal, M. M., Fox, O. D., et al. 2016, ApJ, 833, 231
Tinyanont, S., Kasliwal, M. M., Krafton, K., et al. 2019, ApJ, 873, 127
Tody, D. 1986, Proc. SPIE, 627, 733, doi:10.1117/12.968154
Tody, D. 1993, in ASP Conf. Ser. 52, Astronomical Data Analysis Software and Systems II, ed. R. J. Hanisch, R. J. V. Brissenden, & J. Barnes (San Francisco, CA: ASP), 173
Tolstov, A. G., Blinnikov, S. I., & Nadyozhin, D. K. 2013, MNRAS, 429, 3181
Tonry, J. L., Denneau, L., Heinze, A. N., et al. 2018, PASP, 130, 064505
Vacca, W. D., Cushing, M. C., & Rayner, J. T. 2003, PASP, 115, 389
Valenti, S., Elias-Rosa, N., Taubenberger, S., et al. 2008, ApJL, 673, L155
Veilleux, S., & Osterbrock, D. E. 1987, ApJS, 63, 295
Vreeswijk, P. M., Leloudas, G., Gal-Yam, A., et al. 2017, ApJ, 835, 58
Weaver, T. A., Zimmerman, G. B., & Woosley, S. E. 1978, ApJ, 225, 1021
Wilkinson, D. M., Maraston, C., Goddard, D., Thomas, D., & Parikh, T. 2017, MNRAS, 472, 4297
Woosley, S. E. 2010, ApJL, 719, L204
Woosley, S. E. 2017, ApJ, 836, 244
Woosley, S. E., & Bloom, J. S. 2006, ARA&A, 44, 507
Woosley, S. E., & Heger, A. 2006, ApJ, 637, 914
Woosley, S. E., Heger, A., & Weaver, T. A. 2002, RvMP, 74, 1015
Wright, E. L., Eisenhardt, P. R. M., Mainzer, A. K., et al. 2010, AJ, 140, 1868
Yan, L., Lunnan, R., Perley, D. A., et al. 2017a, ApJ, 848, 6
Yan, L., Quimby, R., Gal-Yam, A., et al. 2017b, ApJ, 840, 57
Yan, L., Quimby, R., Ofek, E., et al. 2015, ApJ, 814, 108
Yaron, O., & Gal-Yam, A. 2012, PASP, 124, 668
Yoon, S.-C. 2017, MNRAS, 470, 3970
Young, D. R., Smartt, S. J., Valenti, S., et al. 2010, A&A, 512, A70
Zackay, B., Ofek, E. O., & Gal-Yam, A. 2016, ApJ, 830, 27